**Final
Project Technical Report
of ISTC 1863-2000**

Experimental study of stability and transition of hypersonic boundary layer around blunted cone

(From 1 November 2000 to 31 October 2001 for 12 months)

**Anatol? Alexandrovich Maslov
(Project Manager)**

Institute of Theoretical and Applied Mechanics

December 2001

REPORT DOCUMENTATION PAGE

Form Approved OMB No. 0704-0188

Public reporting burden for this collection of information is estimated to average 1 hour per response, including the time for reviewing instructions, searching existing data sources, gathering and maintaining the data needed, and completing and reviewing the collection of information. Send comments regarding this burden estimate or any other aspect of this collection of information, including suggestions for reducing the burden, to Department of Defense, Washington Headquarters Services, Directorate for Information Operations and Reports (0704-0188), 1215 Jefferson Davis Highway, Suite 1204, Arlington, VA 22202-4302. Respondents should be aware that notwithstanding any other provision of law, no person shall be subject to any penalty for failing to comply with a collection of information if it does not display a currently valid OMB control number.
PLEASE DO NOT RETURN YOUR FORM TO THE ABOVE ADDRESS.

1. REPORT DATE *(DD-MM-YYYY)*	2. REPORT TYPE	3. DATES COVERED *(From – To)*
04-03-2002	Final Report	27-Nov-00 - 27-Nov-01

4. TITLE AND SUBTITLE

Experimental Study Of Stability And Transition Of Hypersonic Boundary Layer Around Blunted Cone

5a. CONTRACT NUMBER
ISTC Registration No: 1863p

5b. GRANT NUMBER

5c. PROGRAM ELEMENT NUMBER

6. AUTHOR(S)

Dr. Anatoly Maslov

5d. PROJECT NUMBER

5d. TASK NUMBER

5e. WORK UNIT NUMBER

7. PERFORMING ORGANIZATION NAME(S) AND ADDRESS(ES)
Institute of Theoretical and Applied Mechanics
Institutskaya 4/1
Novosibirsk 630090
Russia

8. PERFORMING ORGANIZATION REPORT NUMBER

N/A

9. SPONSORING/MONITORING AGENCY NAME(S) AND ADDRESS(ES)

EOARD
PSC 802 BOX 14
FPO 09499-0014

10. SPONSOR/MONITOR'S ACRONYM(S)

11. SPONSOR/MONITOR'S REPORT NUMBER(S)
ISTC 00-7019

12. DISTRIBUTION/AVAILABILITY STATEMENT

Approved for public release; distribution is unlimited.

13. SUPPLEMENTARY NOTES

14. ABSTRACT

This report results from a contract tasking Institute of Theoretical and Applied Mechanics as follows: Study is devoted to basic research of stability and transition of hypersonic boundary layer around blunted cone. Nosetip bluntness effects have very strong influence on laminar-turbulent boundary layer transition. These effects are very complex because the nosetip-region boundary layer may be under the influence of by-pass phenomena, Tollmien-Schlichting waves, and Goertler vortices. Results of fulfilled stability experiments do not agree with computations. But such a comparison is not at all valid because natural disturbances were studied in former experiments. In the present project the artificial wave-packet method will be applied to get the necessary data for waves for various single incidence angles. Obtained results will be used for a correct comparison between theory and experiment. The experimental investigations will be performed in the blowdown wind tunnel T-326 in Hypersonic Flow Laboratory of ITAM SB RAS at Mach 6. A point-source glow-discharge perturber will be used to excite the boundary layer frequency band corresponding to the first and second mode waves. Mean flow and pulsations measurements will be carried out using hot-wire anemometer. Detailed experimental data on the position of the laminar-turbulent transition, characteristics of natural disturbances and evolution of artificial disturbances in the boundary layer of a cone with different nose bluntness at Mach number M=6 will obtained. The proposed project will allow a bank of experimental data on the stability of the hypersonic boundary layer to be compiled. As a result, a better insight into the processes taking place in hypersonic boundary layers will be gained.

15. SUBJECT TERMS
EOARD, Aviation Technology, Aircraft

16. SECURITY CLASSIFICATION OF:

a. REPORT	b. ABSTRACT	c. THIS PAGE
UNCLAS	UNCLAS	UNCLAS

17. LIMITATION OF ABSTRACT
UL

18, NUMBER OF PAGES

19a. NAME OF RESPONSIBLE PERSON
Wayne Donaldson

19b. TELEPHONE NUMBER *(Include area code)*
+44 (0)20 7514 4299

Standard Form 298 (Rev. 8/98)
Prescribed by ANSI Std. Z39-18

Experimental study of stability and transition of hypersonic boundary layer around blunted cone
(From 1 November 2000 to 31 October 2001 for 12 months)

Anatol? Alexandrovich Maslov (Project Manager)
Institute of Theoretical and Applied Mechanics *

The objective of this project is to basic research of stability and transition of hypersonic boundary layer around blunted cone. Next results is obtained:

-experimental data on the position of the laminar-turbulent transition in the boundary layer of a cone with different nose bluntness for Mach 6;

-experimental data on the characteristics of natural disturbances in the hypersonic boundary layer of a blunted cone for Mach 6; -experimental data on the evolution of artificial disturbances, excited in the hypersonic boundary layer on a blunted cone for Mach 6.

Acquired experimental data could be used for validation of numerical techniques. Using of obtained data will help to more accurate prediction of laminar-turbulent transition location and thereby heat fluxes on hypersonic vehicles.

---

*630090, Novosibirsk, Institutskaya st. 4/1, Russia
Phone +7-(383-2) 30-42-79 Fax +7-(383-2) 34-22-68

E-mail: admin@itam.nsc.ru

**The work has been performed by
the following institutes and collaborators.**

1. Participated institutes:
      1.1 Leading institute:
         Institute of Theoretical and Applied Mechanics
            630090, Novosibirsk, Institutskaya st. 4/1, Russia
            Phone +7-(383-2) 30-42-79 Fax +7-(383-2) 34-22-68
            E-mail: admin@itam.nsc.ru
      1.2 Subcontracted institutes: No

2. Foreign Collaborators
      European Office of Aerospace Reasearch and Development
      223-231 OldMarylebone Road, London, United Kingdom, NW1 5TH
      Phone +44 (0) 20 7514 4953, Fax +44 (0) 20 7514 4960
      Email: rphillips@eoard.af.mil

PROJECT MANAGER

Professor Anatoly Maslov

Deputy Director of ITAM

Address: Institute of Theoretical and Applied Mechanics, Institutskaya st. 4/1, Novosibirsk, 630090, Russia

Telephone: 7-(383-2)-30-38-80

Fax: 7-(383-2)-34-22-68

e-mail: **maslov@itam.nsc.ru**

Principal Investigator:

Alexander Shiplyuk

Senior Researcher, Doctor

Investigators:

Dmitry Buntin

Post graduate student

Eugeny Burov

Post graduate student

Boris Sapogov

Engineer

Abstract

In the present report, we describe some experimental results concerning the development of natural and artificial disturbances in a hypersonic boundary layer ($?_\infty = 6$) on 7°- blunt cone. Described in detail are models studied, equipment, devices used for introducing artificial disturbances into the boundary layer, and testing and adjustment procedures for various components of the experimental equipment employed. Radius of nose bluntness ($R_n=0.75$ mm) was chosen on the base of measurements of laminar-turbulent transition location.

It is shown that:
- entropy layer swallowing occurs upstream first measurement cross-section, in measurement region the mean boundary layer profiles for laminar flow zone are self-similar;
- amplitudes of second mode disturbances in blunt cone boundary layer are essentially smaller than for sharp cone conditions.

Development of artificial wave packets was studied for frequency 275 kHz. At this frequency the second mode had maximal amplitude in spectra of natural disturbances. It was found that 2-D waves are the most unstable. Growth curves were obtained for 2-D waves.

Acknowledgements

Table of Contents

List of Tables

List of Figures

List of Symbols

C_x	longitudinal phase velocity of the wave packet
f	frequency
M	Mach number
P_0	stagnation pressure
P_w	wall pressure
Re	Reynolds number
Re_1	unit Reynolds number
R_n	radius on nose bluntness
SA, SF	amplitude and phase spectra with respect to the transversal wave number $\boldsymbol{b}$
SA_0	value of *SA* for $\boldsymbol{b}$=0
T_0	stagnation temperature
T_w	wall temperature
X, *Y*, *Z*	longitudinal, vertical and transversal coordinates
X_{tr}	longitudinal coordinate of laminar-turbulent transition location
U	velocity
$\boldsymbol{b}$	transversal wave number
$\boldsymbol{d}$	thickness of boundary layer
$\boldsymbol{r}U$	mass flow
$<\boldsymbol{r}U>$	integrate RMS mass flow pulsations
$\boldsymbol{r}U'$	mass flow pulsations
Φ	amplitude and phase of artificial disturbances

Subscript
e   flow parameters at boundary layer edge

1 Introduction

The mechanisms of the laminar-turbulent transition at hypersonic velocities still remain poorly studied. The reasons for that are the complexity of theoretical treatment of hypersonic flows, difficulties arising when experimenting with them, and intricate nature of physical processes, finally giving rise to turbulence. As we pass to hypersonic velocities, from Mach numbers ? ≈ 4-4.5 on, alongside with the vortex instability mode, a new acoustic-type instability (the so-called Mack modes) emerges. Numerical simulations [1] show that, among Mack modes, the second mode is the most unstable one; hence, it is this mode that should be expected to govern the position of the laminar-turbulent transition. Wind-tunnel studies [2, 3, 4] confirm, in general, these data. However, in a number of experiments (see for example [5]) the second mode was shown not to dominate in hypersonic boundary layers. Moreover, no second mode at all was found for the flow conditions of interest in [6], it has also been shown that the laminar-turbulent transition occurred independently of the evolution of acoustic disturbances in the boundary layer. In the available scenario of the laminar-turbulent transition, the development of Mack modes is seriously influenced by the mean-flow features of the boundary-layer flow, which additionally complicates the overall picture of the physical processes in hypersonic boundary layers.

One of the important but insufficient investigated effects in hypersonic boundary layers is a dramatic influence of model nose bluntness on the development of a vortex and acoustic modes and on a laminar-turbulent transition. Leading edge bluntness is crucial important at hypersonic velocities since the level of convective heating is inversely proportional to the square root of a bluntness radius. In a number of experiments [7, 8, 9] the effect of the bluntness radius on a position of the laminar-turbulent transition was studied. It was found that increasing nose bluntness first causes increasing Reynolds number of the transition. With further increasing bluntness, Reynolds number of the transition decreases. This problem is very complicated, the boundary layer in the bluntness region is affected by many factors including non-linear effects, Tollmien-Schlichting waves, and Goertler vortexes. The significant influence on the downstream development of natural disturbances is exerted by an entropy layer. The systematic investigations of the natural disturbances development in the hypersonic boundary layer on a cone with small bluntness degree were carried out in [10]. The investigations have demonstrated that the bluntness of the nose increases the critical Reynolds number and raises the disturbances amplifications rates in unstable region. The results of the experimental researches of hypersonic boundary layers stability which were realized in quiet wind tunnels [11], have coincided qualitatively with the data obtained in the conventional wind tunnels.

The detailed analysis of the available experimental data on the hypersonic boundary layer stability on round cones near zero angle of attack has been performed in [12]. Three experiments have been chosen [4, 10, 13], their results may be used for the comparison with calculations. In these experiments the detailed calibrated measurements of mean parameters and flow pulsations have been made. In [4, 10] the development of natural disturbances have been investigated in an conventional wind tunnel. From the analysis of the experimental data and comparison with calculation it was shown that [12]:

- the mean profiles obtained in these papers are distorted apparently due to probe interference and can not be used in the comparison with calculation;

- the measured amplification rates are rather less than the calculated ones in the region of linear development of the second mode disturbances.

In [13] the development of natural disturbances have been investigated in a quiet wind tunnel. The mean flow profiles and amplification rates of the second mode disturbances, obtained in the paper, agree quite successfully with the calculation results [14]. In this experiment, however, the measurements were carried out with a Constant Voltage Anemometer, for which at that time the systematic studies of the calibration technique had been carried out. Therefore, these data call for further verification.

Thus, in [12] it is shown that the good agreement between the calculations and experiments still remain to be achieved even for the simplest conditions and configurations. That is why S.P. Schneider has initiated the investigations of a linear stage of the disturbances development in the hypersonic boundary layers. These investigations were directed to the numerical methods validation. It was suggested that the experiments should be carried out in a conventional wind tunnel in ITAM (Novosibirsk, Russia) with the controlled disturbances being used, the experiments in a quiet wind tunnel in Perdue University (USA) with the natural disturbances, and then to compare the obtained experimental findings with the stability calculations stability carried out by H. Reed (USA). The experiments were supposed to be done under the absolutely similar conditions. A round blunted cone was chosen as a test configuration. It was supposed that particular emphasis should be placed on obtaining detailed information about the studied mean flow and disturbances characteristics, that high precision and reliability of the experimental datasets must be guaranteed.

This Report presents the results of the experiments carried out in ITAM.

In the work the next main tasks were fulfilled:

Task 1. Manufacturing of universal, multi-purpose experimental models.

Task 2. Determination of the position of the laminar-turbulent transition in the boundary layer on cones with different bluntness radii of their nose part.

Task 3. Study of characteristics of natural disturbances in hypersonic boundary layers on blunted cone.

Task 4. Study of characteristics of artificial disturbances deliberately introduced into hypersonic boundary layers on blunted cone.

2 Experimental equipment and techniques

2.1 Wind tunnel

The experiments were carried out in the hypersonic wind tunnel T-326, ITAM SB RAS. T-326 is a blow down wind tunnel. It is equipped with a one-step perforated ejector. The layout of the tunnel is presented in Fig. 1. The wind tunnel is intended for the investigations within the range of Mach number of M=6 $\div$ 14 and unit Reynolds numbers $Re_1 = (5 \cdot 10^6 \div 70 \cdot 10^6)$ m^{-1}, and for this purpose there is a set of changeable profiled and conic axis-symmetric nozzles.

The maximum pressure in a tunnel settling chamber is of 20 MPa, the pressure in the ejector is of 0.8 MPa, the runtime is up to 30 min. To work at Mach numbers of 6$\div$10, an ohmic heater is used which guarantees the air temperature in the settling chamber of up to 800 K. Open-jet test section has a length of 400 mm with a nozzle end diameter of 200 mm. To carry out the experiments, a mechanism of model injection into a free stream is used, which allows to protect the models and sensors from non-stationary loadings during tunnel starting. The test section of the tunnel is equipped with two optic windows of clear diameter of 220 mm, which are used for model examination and flow visualization with the aid of Schlieren-technique.

Flow parameters in the wind tunnel settling chamber (stagnation pressure P_0 and stagnation temperature T_0) during run were measured and kept at constant values by a regulation system. P_0 was measured with the aid of pressure gage IPD-89008 with measurement ranges of: 1.0 MPa, 1.6 MPa, 2.5 MPa. A nameplate error of pressure gage IPD-89008 is 0.06% of the measurement range. All the presented measurements of P_0 were carried out within the range of 1.6 MPa. T_0 was measured by k-type thermocouple having sensitivity coefficient of $4.024 \cdot 10^{-2}$ mV/grad. The

accuracy of T_0 measurement was of 0.1%. During run the parameters P_0 and T_0 were kept constant with the accuracy of 0.06% and 0.25%, correspondingly.

To increase the lifetime of hot wire and to exclude the effect of dust particles on the measurement results, a gas-dynamic channel of the wind tunnel has been modernized. A block of fine air cleaning (Fig. 2) was installed between the air heater and nozzle. It permitted to keep back the dust particles more than 2 micron size. A filtering element consists of two layers of grids made of stainless steel. The filter has low hydraulic drag and high corrosion resistance and it is able to work at high temperatures up to (350–400) C. The tests have demonstrated that pressure drop on the filter does not exceed 0.03 MPa when the pressure in the settling chamber is of 4 MPa.

2.2 Experimental models

At model designing the following main demands were formulated: it is necessary to situate a source of artificial disturbances in the model, as well as a pressure taps to measure wall pressure P_w distribution and a lot of thermocouples to measure model wall temperature T_w; to study a spatial structure of artificial wave packages, one should provide model rotation. To meet these requirements and simultaneously to guarantee design simplicity and reliability, it was decided to produce two geometrically similar models – a model with pressure taps and a model with disturbance source. To provide a possibility of free variation of nose bluntness and disturbance source replacement, the models consist of three parts: a nose part, a middle part with the built-in disturbance source, and a base part.

The dimensions of the model – length of 500 mm, cone half-angle of 7 degrees, bluntness radius of the nose part of 0.5 mm were chosen basing on the analysis of the available experimental and theoretical data. The model dimensions were agreed with S.P. Schneider to guarantee the possibility of repetition of these investigations in a quite wind tunnel in Perdue University under the same conditions.

The thermocouples were supposed to be situated on the inner side of model wall. To find the thickness of model wall which is suitable to the measurement of model surface temperature, temperature difference between the outer and inner sides of the wall were estimated for different wall thickness. From heat conductivity equation $q = \lambda \dfrac{dT}{dx}$ for the steady conditions we obtain

$\Delta T \approx q \dfrac{\Delta}{\lambda}$, where λ is heat conductivity coefficient (for steel $\lambda = 48$ [J/(m·sec·K)]), q [J·(m²·sec)⁻¹] is the density of convective heat flux which depends on difference in model wall

15

and gas temperatures, Δ [m] is model wall thickness. Let the model wall temperature is minimal and equal to the ambient temperature, the convective heat flux density is maximal and equal to $q_{max} \approx 550$ J/(m^2·sec). Then for $\Delta = 5$?? and q_{max} the temperature difference between the outer and inner sides of the wall is about 0.1°. Here the error of definition of temperature factor $T_w/?_0$ is 0.03%, therefore for these conditions it is possible to assume that the wall is thin enough.

The experiments were carried out at the model temperature close to the recovery temperature. Let us estimate the time of model heating up to the recovery temperature. For this purpose let us use the approach of one-dimension non-stationary heating $mc\dfrac{dT_w}{dt} = sq$. Here $m = 3.5$ kg is model mass, $? = 448$ J·(kg·grad)$^{-1}$ is specific heat capacity for steel, $s = 0.095$?^{2} is model surface area, t – time, q – convective heat flux density. The density of a convective heat flux may be presented as: $q = h(T_{wr}-T_w)$, where $h = 30.2$ J·(m^2·sec·grad)$^{-1}$ is heat transfer coefficient, $?_{wr} = 335.5$? is the recovery temperature on the model wall at $T_0 = 385$? . Integrating this equation, we obtain:

$$\ln(T_{wr} - T_w) = \frac{sh}{mc}t + const , \quad \text{or} \quad t = \ln\left(\frac{T_{wr} - T_{w_0}}{T_{wr} - T_w}\right)\frac{mc}{sh},$$

where T_{w0} – model initial temperature, T_w is the temperature of the model at the time t.

Let us estimate the duration of model heating from temperature $T_{w0} = 300$ K up to the temperature which 1% differs from T_{wr} ($T_w = 332$ K), for these conditions we find that $t = 21$ min. Runtime is of 30 min. One may see that without extra heating the model temperature will reach the needed level only by the end of the run. To assign the temperature regime faster, an external heater was set on the model on the intervals between runs. But model temperature still decreased down to (315–318) K between the runs, because the heater power input was insufficient. At such an initial temperature $t = 15$ min, thus the model had to be heated up additionally at the beginning of each run; to do this, the increased stagnation temperature ($T_0 \sim 450$ K) was held for the first several minutes.

2.2.1 The model with pressure taps

This model is intended for measurement of wall pressure distribution on the model surface and model installation at zero angles of attack and yaw. The model general view is presented in Fig. 3. The position of pressure taps is shown in Fig. 4 and given in Table 1. The first pressure tap is located in the middle part at a distance of 98 mm from the model nose. The distance be-

tween the nearest pressure taps is of 25 mm; an orifice diameter is of 0.6 mm. The pressure taps for wall pressure distribution measurement are situated on the generatrix. Four pressure taps for cone installation at the zero angles are arranged on a radius at antipodal positions at a distance of 148 mm from the model nose. The total amount of the pressure taps is 19. A stainless steel pipe is soldered in each orifice, a flexible hose which goes out of the model end face, is donned on a pipe. The cone with the pressure taps could not be rotated during the run.

To measure the model temperature, there are three thermocouples arranged on the generatrix on the inner side of the wall. The positions of the thermocouples are shown in Table 2.

2.2.2 The model with controlled disturbance source

The model with a source of disturbances is intended for hot-wire measurements of the development of natural disturbances and artificial wave packets in a boundary layer. The general view of the model is demonstrated in Fig. 5. Fig. 6 shows a picture of the model with the source of artificial disturbances which is ready to carry out the hot-wire measurements. Nearby one may see an exchangeable block of point electric-discharge source and four interchangeable nose parts.

To generate the artificial disturbances, two sources were designed and manufactured: a point one to generate the wave packets, and a ring one to generate 2-D waves. The disturbances are generated by a high-frequency glow discharge. The pulsations from the point source are entered into the boundary layer through a orifice of 0.5 mm diameter. The orifice is situated at a distance of 69 mm from the model nose. The pulsations from the ring source are entered through a circular slit of 0.1 mm width, which is situated at a distance of 91.5 mm from the model nose.

To measure the temperature of the model, the thermocouples are situated on the inner side of the wall, along the generatrix. In each middle parts there are two thermocouples and in the tail part there are 10 thermocouples located with a step of 37 mm. Thermocouple positioning is presented in Table 2.

To study the spatial structure of the generated disturbances, the model is able to rotate around its axis. The base of rotation is made maximally long to decrease beating at the rotation. The rotation of the model was carried out by a high-accuracy gearing with the aid of bevel gears. A rotation arbor of the driving gear was arranged perpendicularly to the model axis right after a supporting pylon that protected the rotation mechanism from flow impact.

All the components of the model construction were fitted precisely. The assembled model was turned and polished also in assembly. This procedure allowed to eliminate the joints between the units and to reach the value of model surface roughness of less than 0.5 micron.

2.2.3 Alignment of the model at zero angles

The alignment of the cone along flow axis was achieved using the following procedure. To be adjusted first was the pylon of the model. Rotation unit with mounted on its face mirror was installed on pylon (see Fig. 7). The inclination angle of the mirror to the mounting-face plane of the mirror-rotating unit could be finely adjusted. Further, the settling chamber of the wind tunnel should be removed. Two transparent circular diaphragms with 1.5-mm-diameter central orifice were inserted into the inlet and outlet sections of the nozzle. A laser beam was directed through these openings. By displacing the frame of the pylon, we could hit the center of the mirror by the laser beam. Then, the mirror unit is rotated with simultaneous adjustment of the inclination angle of the mirror to the mounting-face plane of the mirror-rotating unit until the beam reflected from the mirror no longer wobble. After that, the mirror plane was assumed to be normal to the axis of rotation and, hence, to the axis of the drive opening of the pylon. Then, the diaphragm installed at the nozzle exit was removed and, by varying the installation angles of the pylon, we forced the reflected beam fall onto the laser output window. Now, the axis of the rotation unit could be believed coincide to the nozzle axis, and the pylon was to be rigidly fixed to the pylon frame, as well as the pylon frame to the base of the test section of the wind tunnel. Subsequently, the model was installed on rotation unit, and the settling chamber was mounted in its proper place. Such an alignment procedure ensured coincidence between the model axis and the wind direction within 0.05 degrees.

2.3 Traverse system

Wind tunnel T-326 is equipped with a three-component traverse system which provides the accuracy of 0.01 mm in motion over coordinates *X, Y, Z*.

To rotate the models around the longitudinal axis, an rotate unit is used. It guarantees the accuracy of turning of 0.1^o.

The model and the traverse units are installed on a frame (Fig. 8). Model surface can be located by an electric contact switch. This enables the computer to stop the traverses at known location before the hot-wire reaches the surface.

2.4 Hot-wire anemometer system

2.4.1 Constant temperature anemometer

In present work an AN-1003 constant temperature anemometer (CTA) with option 04 (frequency compensation) was used. It is manufactured by A.A. Lab Systems, Israel.

Features

- Easy operation.
- Low Noise - less than 2.2 nV/$\sqrt{Hz}$.
- Ultra Low Noise option - less than 400pV/$\sqrt{Hz}$.
- Intelligent modular design.
- CTA and CCA in a single channel (optional).
- Probe protection circuit.
- Soft-start circuit for delicate probes.
- High frequency response: DC-100k Hz standard, DC-500 kHz optional (option 04).
- Flexible: may be used with Hot-film and Hot-wire.
- Built-in Signal Conditioner :
    - Controllable Gain,
    - DC offset, adjustable to any value,
    - Noise Filter: Low Pass Filter with 12 cut-off frequencies.
- Built-in indicators aid user in balancing the Bridge.
- Built-in Square Wave/Pulse Generator.
- Fail-safe switches.
- Self-maintained, no expensive servicing required.
- 12-months Parts & Labor warranty.

The typical frequency response for AN-1003 Hot-Wire Anemometer with options 01 (**ULTRA LOW NOISE INPUT AMPLIFIER**) & 04 (**FREQUENCY COMPENSATION**) is shown in Fig. 9. The amplitude is relative to the 1 kHz amplitude. This picture was taken from official web-site of **A.A. LAB SYSTEMS (www.lab-systems.com).**

2.4.2 Constant current anemometer

In present work a constant current anemometer (CCA) manufactured in ITAM was used. The CCA consists of two main circuits:

- the low-frequency (0–10 Hz) circuit to provide constant mean resistance of a hot-wire;

- the high-frequency (<500 kHz) compensating amplifier to overcome degradation of hot-wire sensitivity with increasing of frequency.

2.4.3 Hot-wire sensor

The measurements were carried out with a single-component hot-wire sensor made of tungsten wire of 1 mm length and 5 micron diameter.

2.5 System of measurement control and data acquisition

System of measurement control and data acquisition structurally consists of two parts: 1) system of free stream parameters control, of mean parameters (P, T…) measurement and traverse system device operating; 2) computer hot-wire system.

1) System of control of free stream parameters, of mean parameters measurement and traverse system device operating. The free stream parameters are determined by P_0 and T_0 measurement. To measure P_0, T_0, P_w, T_w ADC PCI-9114HG (© ADLINK Technology Inc., Taiwan) PC data acquisition card is used. It provides the following advanced features:

- 16 differential analog inputs;
- 16 bits high resolution AD conversion;
- sampling rate up to 100 kHz;
- input range: ±10V, ±1 V, ±0.1 V, ±0.01 V.

The signals from each sensors and thermocouples were digitized with the frequency of 30 kHz. Each 512 samples were averaged and the mean values were stored in personal computer memory.

Traverse gears operating was carried out by a personal computer or by manually through by means of the control device.

The software developed for this part of the measurement system is allowed experimentalist to monitor during the run the free stream parameters, to operate the traverse gears, to record the experimental data and to start up the hot-wire measurements system.

2) Computer hot-wire system. This system consists of a personal computer and PCI-9812 (© ADLINK Technology Inc., Taiwan) PC data acquisition card. This ADC provides the following advanced features:

- 4 single-ended analog input channels;
- 12-bit analog input resolution;
- Up to 20MHz A/D sampling rates;

- 4 A/D converters, one converter for each analog channel;
- Trigger Sources: Software, Analog threshold comparator using internal D/A to set trigger level, and External digital trigger.

During natural disturbances measurements by CTA, 1 time-series of 5242886 samples each were acquired at each measurement station, with sampling rate of 1 MHz. During natural disturbances measurements by CCA, 1 time-series of 401408 samples each were acquired at each measurement station, during measurements of artificial disturbances – 98 time-series of 4096 samples at each measurement station. Analog signal of main generator initiating the glow discharge was used to trigger ADC. Since the output signal of CCA had a high level of high-frequency signals, the sampling rate was increased up to 5 MHz to avoid aliasing.

The software allows to process the data obtained (spectra, amplitude and phase characteristics of the artificial disturbances) in the real time and to plot them on a monitor. The information about the parameters of the artificial disturbances, sensor locations and free stream characteristics during run were saved to a hard disk of the personal computer. At the same time an experimental program is controlled by the second computer, and the information exchange between computers is realized by Ethernet, protocol TCP/IP. Thus, the process of experiment is automated completely and may be carried out without experimentalist participation.

2.6 The system of high-frequency glow discharge

The system consists of a clock generator and high-voltage generator. The signal of the clock generator is used to initiate the high-voltage generator and to synchronize hot-wire measurements with the high-voltage generator starting up. The high-voltage generator produces voltage pulses up to 2000 V, of 1 microsecond duration and pulse frequency up to 400 kHz. In the course of the run the discharge glow is controlled visually through optic windows and a mirror in the test section.

Ring and point sources were tested in hypersonic flows. During testing the electrode shapes were optimized to improve efficiency of glow discharge. Also new circuit providing more power, higher frequency range and less electric interference with hot-wire was successfully examined.

2.7 Processing of wave characteristics of the disturbances

To obtain amplitude (A) and phase (F) of the controlled disturbances, discrete Fourier transformation was used:

$$A(X,Y,\boldsymbol{q})e^{i\Phi(X,Y,\boldsymbol{q})} = \frac{2}{N}\sum_{j=1}^{N}\boldsymbol{r}\,U_n(X,Y,\boldsymbol{q},t_j)e^{-i\boldsymbol{w}t_j}\;,$$

where N is the samples count in the time-series, $\boldsymbol{w}$ is the frequency of controlled disturbances, $\boldsymbol{r}U_n(X,Y,\boldsymbol{q},t_j)$ is the time-series of mass flow pulsations.

To compare the experimental and calculation data, the artificial wave packet must be presented as a set of waves. For this purpose the transversal wave spectra were computed:

$$SA(x,\boldsymbol{b})e^{iSF(x,\boldsymbol{b})} = \int_{-\boldsymbol{q}_0}^{\boldsymbol{q}_0} A(x,\boldsymbol{q})e^{i\Phi(x,\boldsymbol{q})}e^{-i\boldsymbol{b}\boldsymbol{q}}d\boldsymbol{q}\;,$$

where SA, SF – are the amplitude and phase spectra with respect to the transversal wave number $\boldsymbol{b}$.

2.8 The measurements in a free stream

To check the flow field, the measurements of distribution of Pitot pressure, static pressure, total temperature, and mass flow pulsations were carried out in the free stream. Picture of combined probe for free stream measurements is shown in Fig. 10. The picture of the tunnel test section with the three-component traverse system and combined probe is given in Fig. 11. The example of free stream parameters distributions over transversal coordinate Z is shown in Fig. 12.

2.9 Measurement of temperature and pressure on the model wall

The measurement of pressure P_w on the model surface were carried out with the aid of differential pressure gage TDM4-D. The measuring range of the sensors was of 10 kPa, the sensitivity coefficient – $3.32 \cdot 10^{-3}$ mV/Pa. The sensors were arranged inside the test section of the wind tunnel, to decrease the length of supply pipes. To avoid the temperature impact on sensors signals, they were thermally insulated. The standard error of wall pressure measurement was of 1% of measured values.

The distributions of temperature T_w on the model surface were measured by T-type thermocouples. Their locations is given in Table 2. The sensitivity coefficient of the thermocouples was of $4.053 \cdot 10^{-2}$ mV/grad. The standard error of measurement was of 0.1%.

2.10 The procedure of artificial disturbances measurement

Fig. 13 presents schematically the procedure of measurements.

Measurement stages:

- Touch. The hot-wire moved down to the touching of the electrical contact to the model surface;

- Vertical distribution. The hot-wire moved vertically up. The measurements were carried out with the step of 0.03 mm at a distance of 0.9 mm, then with the step of 0.05 mm at a distance of 1 mm, and then with the step of 0.1 mm at a distance of 2 mm;

- Transversal distribution. The hot-wire moved vertically down in pulsation maximum. The position of maximum was defined at the previous step. Then the model was rotated within the angles range of $\theta = -35^0 \div 35^0$. The measurements were carried out with the step of 0.5^o;

- The model was rotated back in position $\theta = 0$. Then the hot-wire moved stepwise at a distance of 25 mm. The step size was of 5 mm by X, 0.6 mm by Y. At each step the hot-wire crossed the layer of maximum pulsations twice. The measurements were carried out with the step of 0.25 mm by X, 0.05 mm – by Y;

- Then the procedure repeated.

3 Results of measurements

3.1 Wall pressure measurement

Due to the limited amount of differential channels of PCI-9114HG ADC (16 channels in all) it was impossible to measure static pressure in each of 19 pressure taps in one run. Thus two runs were carried out. In the first one the pressure was measured in the pressure taps with odd numbers, in the second – in the taps with even numbers. The exception was four pressure taps (3, R1-R3) which are located in antipode positions in one cross section at $X = 148$ mm. In these points the measurements were carried out in both runs. The free stream parameters for the wall pressure measurement are presented in Table 3. The temperature of the model during the experiment was controlled with thermocouples d1–d3. Their positions are given in Table 2.

Fig. 14 presents the distribution of P_w obtained in two runs in the antipode points in cross section $X=148$ mm (taps 3, R1-R3), also there are the standard errors for measurement presented. The angles of model installation were calculated by this pressure distribution. It was obtained that the measurements were carried out on the windward surface; the angle of attack and angle of yaw were of 0.04 ± 0.06^o and 0.07 ± 0.06^o, correspondingly.

The deformation of a bow shock wave appears due to model nose bluntness, and this deformation results in distortion of wall pressure distribution near the model nose. At $X/R>100$ this dis-

23

tortion disappears and the pressure along the cone surface becomes constant. The first pressure tap is located at a distance of 92.6 mm from the model nose. Thus, the measurement was carried out in the region of constant P_w. The distribution of the pressure over the cone generatrix is shown in Fig. 15. The mean pressure on the cone surface is $P_w \approx 1240$ Pa. The P_w deviation from the mean value does not exceed 2.5%. Data scattering may be caused by free stream nonuniformity in the measurement region. The obtained value of P_w well agreed with the calculated value ($P_w = 1270$ Pa). The calculation was done for a sharp cone in non-viscous approach.

3.2 Measurement of laminar-turbulent transition location in a boundary layer on a cone with different nose bluntness

The location of a laminar-turbulent transition X_{tr} was defined by the thermocouple measurements of the distribution of model wall temperature T_w. The free stream parameters and the results obtained are presented in Table 4. The measured distributions of T_w are shown in Fig. 16. The measurements were carried out for $R_n = 0, 0.5, 0.75$ mm. The dependence of X_{tr} on nose radius is given in Fig. 17. X_{tr} is 4% increased for $R_n = 0.5$ mm in comparison with X_{tr} for the sharp nose. X_{tr} is 9% increased for $R_n = 0.75$ mm. The further measurements of mean and fluctuations characteristics of the boundary layer were carried out on a model with nose radius of 0.75 mm. The picture and sizes of a spherical bluntness are presented in Fig. 18.

3.3 Model wall temperature

An example of temperature factor T_w/T_0 distribution over the generatrix for one run is shown in Fig. 19. The experimental data are shown with symbols. Lines 4, 5 correspond to adiabatic wall conditions for the laminar ($T_w/T_0 = 0.87$) and turbulent ($T_w/T_0 = 0.91$) boundary layers. The variation of model temperature during run was insignificant. The temperature factor in the laminar region ($X < 300$ mm) was of 0.86 ± 0.02 for all runs.

3.4 Measurement of natural disturbances characteristics by CTA

The measurements of boundary layer mean parameters and natural disturbances characteristics were carried out with CTA technique. Distributions across the boundary layer were measured in 10 cross sections with a step of about 30 mm within the range of $X=107$–365 mm in the laminar, transition, and turbulent regions. The obtained dependencies of mass flow (rU), velocity (U), and integral RMS pulsations of the mass flow ($<rU>$) on a vertical coordinate Y are shown in Fig. 20, Fig. 21, Fig. 22, correspondingly. The same distributions are presented in Fig. 23, Fig. 24, Fig. 25 in a dimensionless form. The mass flow and velocity were normalized to the val-

ues at the edge of the boundary layer, Y was normalized to boundary layer thickness d. For clearance the locations of measurement cross sections are shown in Fig. 26.

The distance where the entropy layer is swallowed by the boundary layer, X_{swal} for $R_n = 0.75$ mm is equal to 110 mm. X_{swal} was calculated by formula [15]:

$$\frac{X_{swal}}{(\mathrm{Re}_{1\infty})^{1/3}(R_n)^{4/3}} \approx 7 \;.$$

For the measured cross sections $X=107–365$ mm $\geq X_{swal}$, i.e. in the measurement region the entropy layer is swallowed completely by the boundary layer. The profiles $rU/(rU)_e$, U/U_e for $X=107–304$ mm are similar and close to the calculated profiles for the laminar boundary layer. At $X=334, 365$ mm the profiles are filled which points to the beginning of laminar-turbulent transition. The profiles $<rU>$ at $X=107–273$ mm have the shape typical for the hypersonic boundary layers with the typical maximum situated at $Y/d \approx 0.8$. At $X=304, 334, 365$ mm fast increase of pulsation amplitude takes place, pulsation peak expanses and the position of maximum begins to near to the wall which also points to the beginning of laminar-turbulent transition.

Fig. 27 demonstrates the spectra of mass flow pulsations in the layer of maximum pulsations within the range of $X=190–365$ mm. The level of low-frequency pulsations (~1 kHz) is 1000 higher than the amplitude of high-frequency (200–300 kHz) pulsations. The voltage resolution of ADC was insufficient for the pulsations with frequencies higher than 300 kHz. At boundary layer turbulization the amplitude of high-frequency disturbances rise faster than of low-frequency ones but their level remains much (aprox 1000 times) lower.

3.5 Comparison of CTA and CCA

In the paper presented, to study the characteristics of second mode disturbances, it was necessary to carry out the measurement of pulsations at frequencies up to 300 kHz. CTA has a number of advantages in comparison with CCA in measuring with high overheat: the calibration and measurement techniques are easier, the automatic compensation of sensor thermal inertia does not require account of variation of sensor time constant across the boundary layer. In the first part of the work AN-1003 CTA was used. The description of this hot-wire anemometer is given above. While measuring natural disturbances spectra with CTA, a strong fall of the amplitude with frequency increasing was obtained (Fig. 27). For example, for 10 times frequency change (from 10 kHz to 100 kHz) the amplitude decreases 100 times. At high frequencies ($f > 300$ kHz) a useful signal became less than the electric noise of CTA, and only CTA noise was measured. The value

of CTA noise was constant and did not depend on frequency. As is known (see, for example [16]), the hot-wire anemometer noise amplitude must increase proportionally to frequency.

After the first series of the experiments with CTA AN-1003 it was decided to check accurately all the technique of hot-wire measurements. For this purpose a jet facility was used. This facility works continuously and thus it was possible to adjust accurately and check in detail the signal of different hot-wire anemometer under the similar conditions. The measurement of pulsation spectra were carried out in the shear layer of supersonic jet. Unfortunately the installation was operated only at relatively small pressure of P_0=100 kPa, therefore in the shear layer the high-frequency (> 50 kHz) pulsations were absent. The following hot-wire anemometers were used:

1. AN-1003 CTA (the description is given above);

2. CTA manufactured in ITAM. The circuit of this anemometer is similar to AN-1003 circuit. Frequency range is of 800 kHz;

3. CCA manufactured in ITAM. Frequency range is of 75 kHz;

4. CCA manufactured by the authors. This CCA consisted of a Whitestone bridge only and did not include a compensation amplifier. To compensate a hot-wire signal, the time constant was measured with the aid of a harmonic signals generator, the compensation of time constant was carried out during computer processing of CCA signal.

The obtained pulsations spectra are presented in Fig. 28. The designations on the plot correspond to the numbering of hot-wire anemometers given before. Symbols 5 indicate a signal of hot-wire included into the CCA bridge without compensation of time constant. The spectra obtained with CTA agreed closely to each other. The spectra obtained with CCA agreed closely to each other too. It confirms that the hot-wire measurements were carried out correctly. The differences between CCA and CTA spectra are very big: at f=1 kHz the amplitudes are practically equal, at f=10 kHz CCA signal is 6 time higher than CTA signal, at f=50 kHz this difference is 65 times. At high frequencies of 30–50 kHz CTA signal coincides with the signal of the non-compensated hot-wire.

The comparison measurement with different hot-wire anemometers were done in many works. In [17] the disturbances in a free stream were measured with CCA and CTA. The difference between CCA and CTA in the integral level of mass flow pulsations ran up to 50%. In [18] the pulsations in the supersonic boundary layer were measured with CVA, CCA, and CTA. DISA Streamline 90C10 CTA with a symmetric bridge was used in this measurements. The successful

agreement of spectra of CVA and CCA was obtained. CTA spectrum coincided with CCA and CVA only for the frequencies lower than 40 kHz. At increasing frequency higher than 40 kHz the relative signal of CTA decreases fast, at 400 kHz CTA signal differs in 10^4 times from CCA and CVA signals.

The main difference between CTA and another types of anemometers lies in the presence of feedback loop. Therefore the pulsation spectra were measured with AN-1003 CTA for different feedback adjustment. The results are given in Fig. 29. CTA was adjusted according to a user manual. First the minimum duration of response impulse was reached, the frequency range of AN-1003 here was maximal (≈500 kHz). With this set-up a signal spectrum was measured (symbols 1). Then the duration of the response impulse was increased (the frequency range of hot-wire anemometer decreased) and the spectra were measured (symbols 2 – 5). At the correct operation of the feedback loop in CTA the variation of the frequency range of CTA should not influence the spectrum within this frequency range. The results obtained show that the amplitude of CTA spectrum increases together with frequency range decrease and nears to the amplitude of CCA spectrum. It means that the high frequency range of the tested CTA results from decreasing amplification factor in the feedback which appears apparently because of incorrect procedure of feedback adjustment. At the correct feedback adjustment the frequency range of these CTA is considerably less and seemingly does not exceed 100 kHz. Extra investigations and the analysis of mathematical model are needed to correct the situation and to guarantee accuracy of CTA measurements.

To carry out further measurements, a new CCA with frequency range of 500 kHz was manufactured. The brief description of this hot-wire anemometer is given above. To check CCA, the natural disturbances spectra were measured in the hypersonic boundary layer on a sharp cone. Fig. 30 demonstrates the spectra measured at pulsation maximums at X=192.8, 217.8, 242.9, 268.0, 293.0 mm (symbols 1-5, correspondingly). The measurements were carried out at the same free stream parameters as in the experiments on the blunted cone. The data obtained show the dominance of second mode disturbances. The spectra qualitatively coincide with the data of [19].

3.6 Study of natural disturbances characteristics with CCA

The stream parameters with which the measurements were carried out, are given in Table 6. The obtained distributions of U, rU, $<rU>$ by Y coincide with the distributions measured with CTA. The spectra of mass flow rate pulsations in the layer of maximum pulsations are shown in Fig. 31. Symbols 1–5 correspond to X=186.0, 210.3, 235.5, 260.8, 286.0 mm. The dramatic dif-

ference is evident in the natural pulsations spectra on the sharp and blunted cones. On the blunted cone the first mode disturbances have rather less amplitudes, the first mode dominates, the second mode disturbances are practically absent, and only in the last section a peak of second mode pulsations appears within the frequency range of 270–280 kHz.

3.7   Study of development of the artificial disturbances at f=275 kHz

The artificial disturbances were generated in the boundary layer at a frequency of 275 kHz, and at this frequency the second mode had maximum amplitude in the natural disturbances spectra.

Fig. 32, Fig. 33, Fig. 34, Fig. 35, Fig. 36 present the examples of distributions of E, $<\boldsymbol{r}U>$, amplitude $\boldsymbol{r}U$', phase, real (Re) and imaginary (Im) parts by Y in the center of a wave packet, correspondingly. The distribution of pulsation amplitude has the maximum at the same Y for natural and artificial disturbances. Out of the boundary layer value A decreases down to 0 fast.

Fig. 37, Fig. 38, Fig. 39, Fig. 40 show the examples of dependence of E, $<\boldsymbol{r}U>$, amplitude $\boldsymbol{r}U$', phase on X for step measurements. Within the range of X in the boundary layer a weak (30%) increase of integral level of natural disturbances $<\boldsymbol{r}U>$ takes place, the amplitude of artificial disturbances increases dramatically (15 times). The phase in the wave packet center within the range of X=250–290 mm changes linearly with small steps. The steps appear due to the fact that the measurements are carried out at various relative heights ($Y/\boldsymbol{d}$) in the boundary layer. From these data a value of longitudinal phase velocity of the wave packet C_x=735 m/sec $\pm$ 0.2% was obtained. The normalized value of C_x/U_e=0.907 is higher than the value for acoustic disturbances (C_x/U_e=0.811). At lower values of X (X<250 mm) the amplitude of artificial disturbances outside the critical layer became close to zero, and the information about the phase was lost.

In Fig. 41, Fig. 42 one may see the examples of transversal distributions of amplitude $\boldsymbol{r}U$', and the phase. The amplitude and phase distributions are near-symmetric and similar for all cross sections. The amplitude distribution has the maximum at the wave packet center. The phase distributions are situated closer in the plot for obviousness. Actually (see Fig. 40), the phase difference between the neighbour sections is of 60 rad. In Fig. 43 there are the amplitude wave spectra (SA) with respect to the transversal wave number $\boldsymbol{b}$. These data were obtained after discrete Fourier transformation of the transversal distributions given in Fig. 41, Fig. 42. As is known from the calculations, the second mode disturbances are mostly unstable at $\boldsymbol{b}$=0. The whole wave packet lies within the range of $\boldsymbol{b}$=$\pm$0.5 rad/degree which approximately corresponds to the range of wave vector inclination angles of $\pm$20$^{\mathrm{o}}$.

Totally there were 5 runs carried out with the measurement of characteristics of the artificial wave packets. The results obtained in each run were similar to the data presented above. All the obtained values of amplitudes at b=0 (SA_0) are given in Fig. 44 in a logarithmic scale regard to X coordinate. Symbols 1–5 mean the data obtained in different runs. The initial amplitude of generated wave packets differed in different runs. The amplitude decreased fast with X decrease, therefore to carry out measurements in the part X=185–210 mm the initial amplitude of artificial disturbances was increased significantly. To compare the amplification rates, normalized SA_0 are presented in a logarithmic (Fig. 45) and a linear (Fig. 46) scales. All the runs resulted in the same growth of SA_0. The plot shown in Fig. 46 agree successfully with the plot for the step measurements (Fig. 40). To demonstrate how fast the growth of the second mode disturbances realizes, Fig. 47 presents the dependence of SA_0 on X at the linear scales, and X range corresponds to the model length. Fig. 48 shows the comparison of SA_0 for the sharp and blunted cones depending on X. The spectra and behavior of high-frequency natural disturbances differ dramatically for the sharp (Fig. 30) and blunted (Fig. 31) cones. The amplification of the artificial disturbances for the sharp (Fig. 48 symbols 6) and blunted (Fig. 48 symbols 1–5) are closely related to each other. The region of instability for the second mode disturbances on the blunted cone is likely to be shifted a little towards the big values of X. The considerable difference in the natural disturbances is evidently caused by the different receptivity conditions and by the development of the disturbances at low Reynolds numbers on the sharp and blunted cones.

4 Conclusions

Experimental investigation of natural and artificial disturbance development in hypersonic boundary layer on blunt cone was carried out at Mach number M=5.95 and unit Reynolds number Re_1=12·10^6 1/m.

Radius of nose bluntness (R_n=0.75 mm) was chosen on the base of measurements of laminar-turbulent transition location.

Mean boundary layer parameters measurement showed that entropy layer swallowing occurs upstream first measurement cross-section, in measurement region the mean boundary layer profiles for laminar flow zone are self-similar.

Natural disturbance spectra were measured. It was obtained that amplitudes of second mode disturbances in blunt cone boundary layer are essentially smaller than for sharp cone conditions. Development of artificial wave packets was studied for frequency 275 kHz. At this frequency the second mode had maximal amplitude in spectra of natural disturbances. It was found that 2-D waves are the most unstable. Growth curves were obtained for 2-D waves.

5 Tables

Table 1. Locations of pressure taps

Number of pressure tap	Distance from model nose, mm
1	92.6
2	117.6
3	142.6
4	167.6
5	192.6
6	217.6
7	242.6
8	267.6
9	292.6
10	317.6
11	342.6
12	367.6
13	392.6
14	417.6
15	442.6
16	467.6
R1	142.6
R2	142.6
R3	142.6

Table 2. Locations of thermocouples

Thermocoupler	Distance from model nose, mm
Model with pressure taps	
d1	120
d2	335
d3	425
Middle part with point source	
s1	76.7
s2	120
Middle part with ring source	
s3	120
Tail part of model with controlled disturbance source	
b1	150
b2	172
b3	213
b4	247
b5	283
b6	325
b7	353
b8	387
b9	420
b10	452

Table 3. Experiment conditions for wall pressure measurements

? ???	$?_0$, ???	$?_0$, ?	Re$_{1\infty}$, 10^6 ?$^{-1}$	? ???????? ???????????	? ???????? ??????????? ??????? (????? ????????? ?????????)
1.1	987	397	11.62	d1, d2, d3	1, 3, 5, 7, 9, 11, 13, 15, R1, R2, R3
1.2	987	396	11.65	d1, d2, d3	2, 3, 4, 6, 8, 10, 12, 14, R1, R2, R3

Table 4. Experiment conditions for transition measurements

Run	$?_0$, kPa	$?_0$, K	Re$_{1\infty}$, 10^6 m^{-1}	Thermocouples	Nose radius, mm	Location of transition, mm
2.1	1000	395	11.7	s1, s2, b1-b10	< 0.1	395
2.2		395		s1, s2, b1-b10	0.5	410
2.3		397		s1, s2, b1-b10	0.75	435
3.1	1000	393	11.8	s1, s2, b1-b10	0.75	432
3.2	1000	395.4	11.7	s1, s2, b1-b10	0.75	428
3.3	1000	390.2	11.9	s1, s2, b1-b10	0.75	430
3.4	1000	394.1	11.7	s1, s2, b1-b10	0.75	430
3.5	1000	392.5	11.8	s1, s2, b1-b10	0.75	435

Table 5. Experiment conditions for natural disturbance measurements with CTA

Run	$?_0$, kPa	$?_0$, K	Re$_{1\infty}$, 10^6 m^{-1}	Thermocouples	Profiles locations (X, mm)	Measurements in maximum pulsations layer (X, mm)
3.1	1000	393	11.8	s1, s2, b1-b10	107	–
3.2	1000	395.4	11.7	s1, s2, b1-b10	107, 140	107–140
3.3	1000	390.2	11.9	s1, s2, b1-b10	107, 136, 166	107–190
3.4	1000	394.1	11.7	s1, s2, b1-b10	190, 227, 257	190–288
3.5	1000	392.5	11.8	s1, s2, b1-b10	273, 304, 334, 365	273–365

Table 6. Experiment conditions for pulsations measurements with CCA

Run	$?_0$, kPa	$?_0$, K	$Re_{1\infty}$, 10^6 m^{-1}	Thermocouples	Profile locations (X, mm)
4.1	999610^{+1140}_{-980}	$385.1^{+1.2}_{-0.8}$	12.1	s1, s2, b1-b10	285.98
	999656^{+1104}_{-1307}	$384.5^{+0.7}_{-0.4}$	12.2		260.69
4.2	999567^{+722}_{-943}	$385.9^{+1.7}_{-0.6}$	12.1	s1, s2, b1-b10	260.59
	999615^{+1057}_{-1043}	$384.8^{+0.7}_{-0.7}$	12.2		235.28
	999633^{+1463}_{-1256}	$384.4^{+0.5}_{-0.6}$	12.2		210.15
4.3	999518^{+482}_{-718}	$381.9^{+1.9}_{-0.7}$	12.3	s1, s2, b1-b10	185.98
	999462^{+738}_{-1030}	$380.5^{+0.8}_{-0.7}$	12.3		211.25
4.4	999523^{+2385}_{-1149}	$384.4^{+2.1}_{-6.9}$	12.2	s1, s2, b1-b10	285.98
	999509^{+707}_{-850}	$386.0^{+0.8}_{-0.7}$	12.1		260.75
	999591^{+931}_{-875}	$386.5^{+1.1}_{-0.6}$	12.1		235.5
	999764^{+1069}_{-764}	$387.0^{+0.1}_{-0.1}$	12.1		210.28
4.5	999482^{+1165}_{-1652}	$383.0^{+1.6}_{-0.9}$	12.2	s1, s2, b1-b10	221.98
	999701^{+1308}_{-1460}	$385.3^{+0.8}_{-1.2}$	12.1		237.11
	999477^{+662}_{-736}	$385.5^{+0.2}_{-0.2}$	12.1		252.29

6 Figures
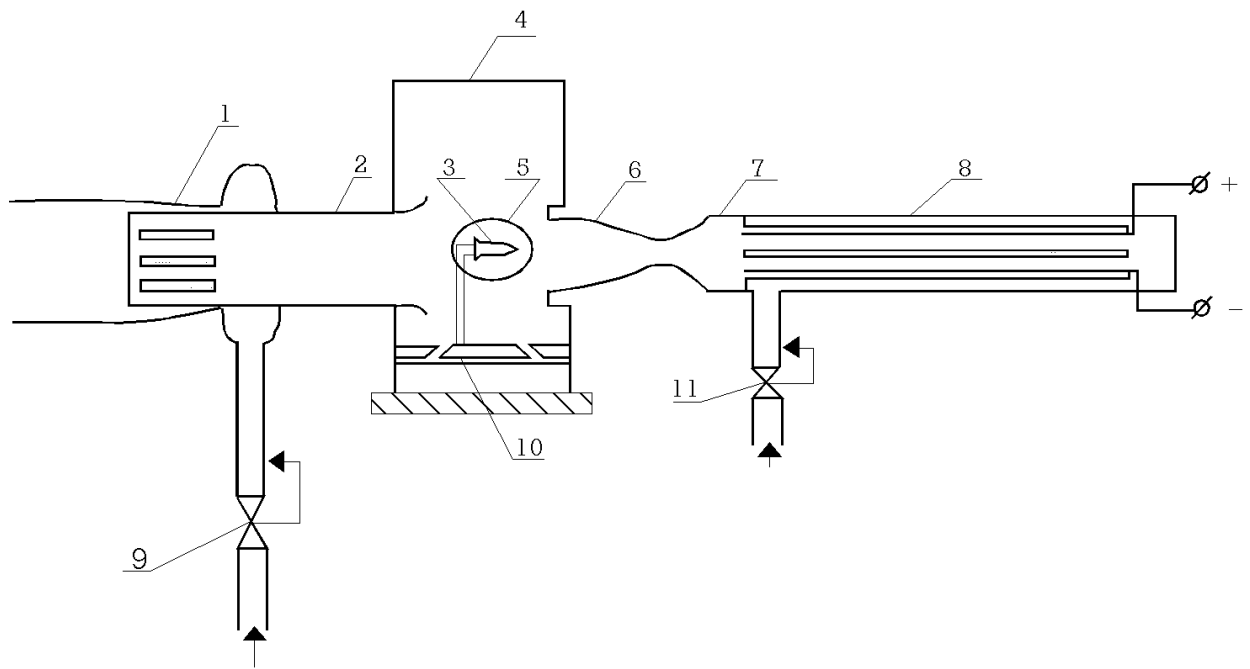
Fig. 1. Scheme of hypersonic wind tunnel T-326 ITAM SB RAS.

1- ejector, 2- diffuser, 3-model, 4- open-jet test section, 5-optical windows, 6- axisymmetric nozzle, 7- prechamber, 8-heater, 9,11-control valves, 10-device to put model into free stream.

Fig. 2. Photo of air-cleaning unit.
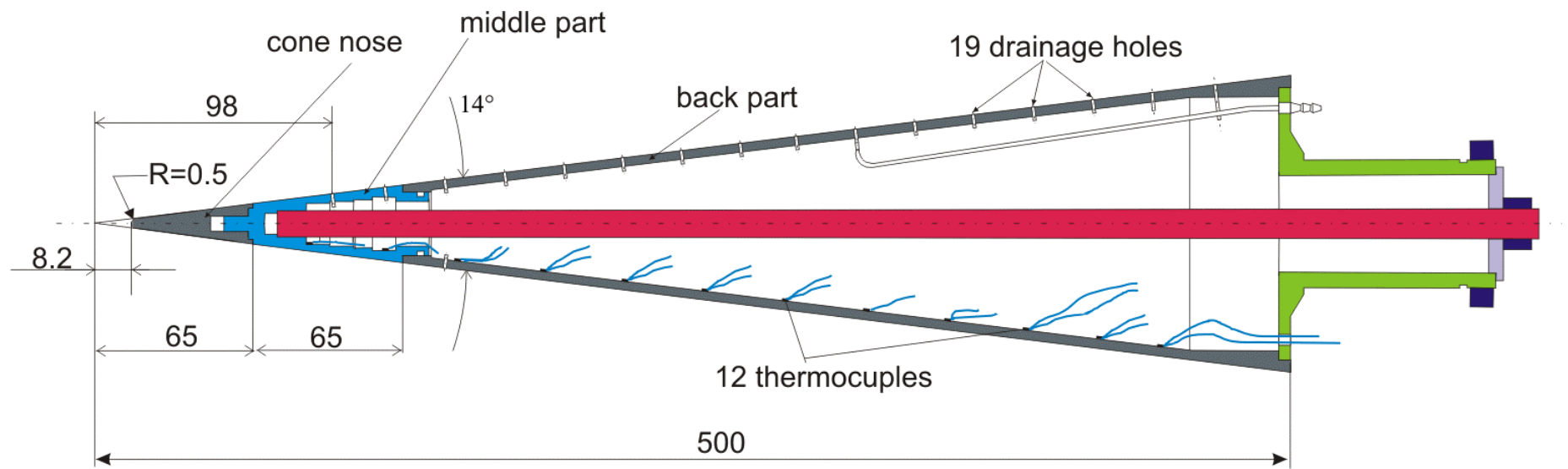
Fig. 3. General view of model with pressure taps.
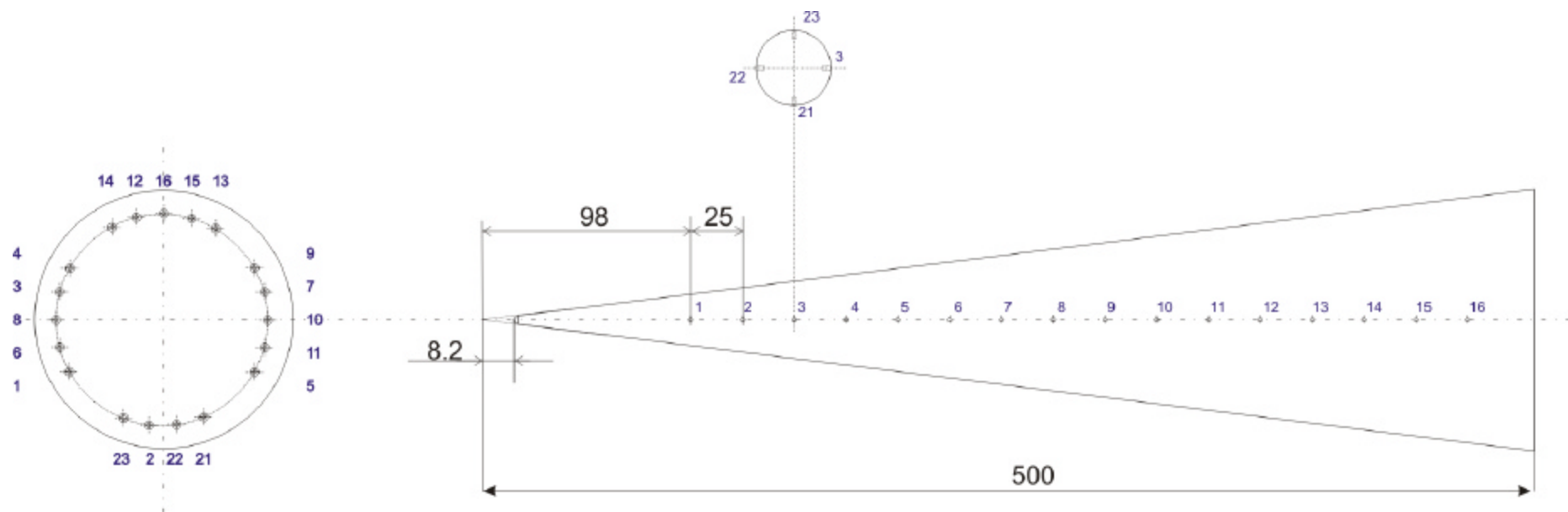
Fig. 4. Pressure taps locations.
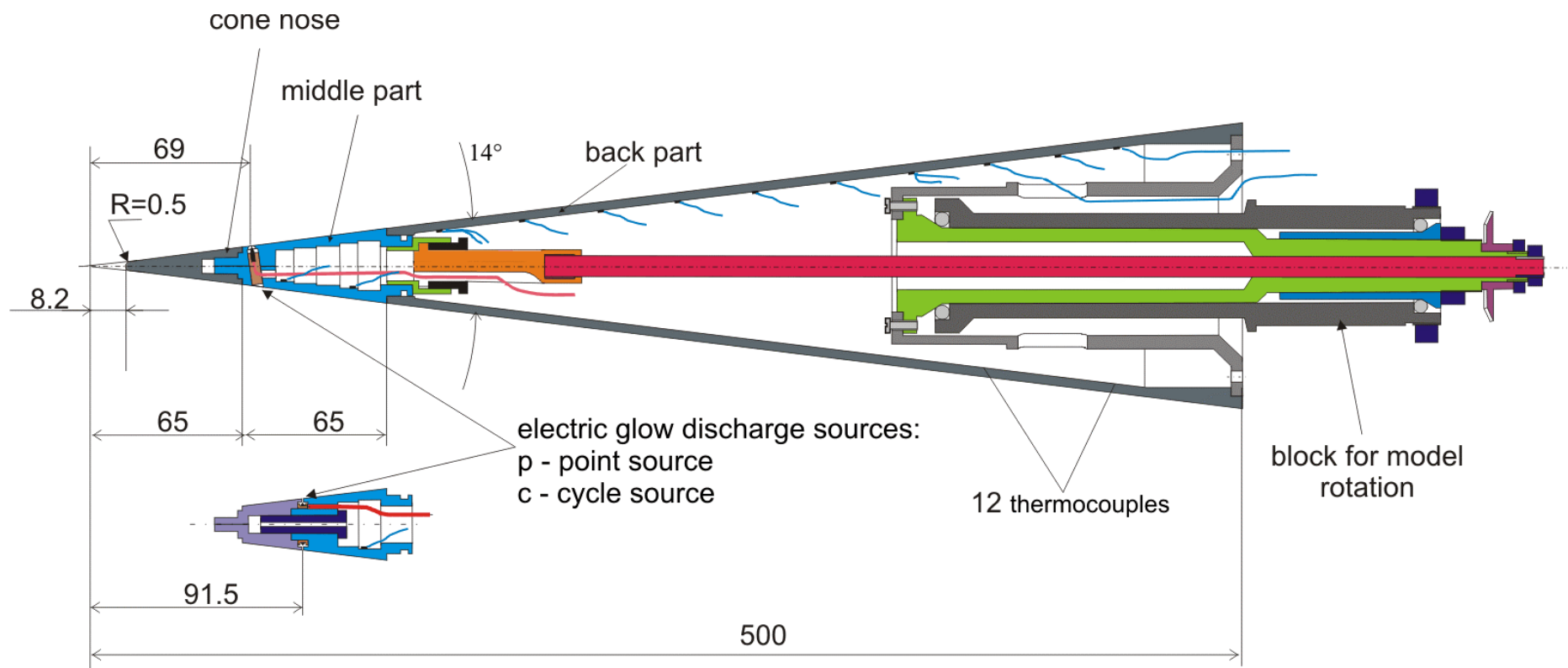
Fig. 5. General view of model with disturbance sources.

Fig. 6. Photo of model with disturbance sources and exchangeable nose parts.
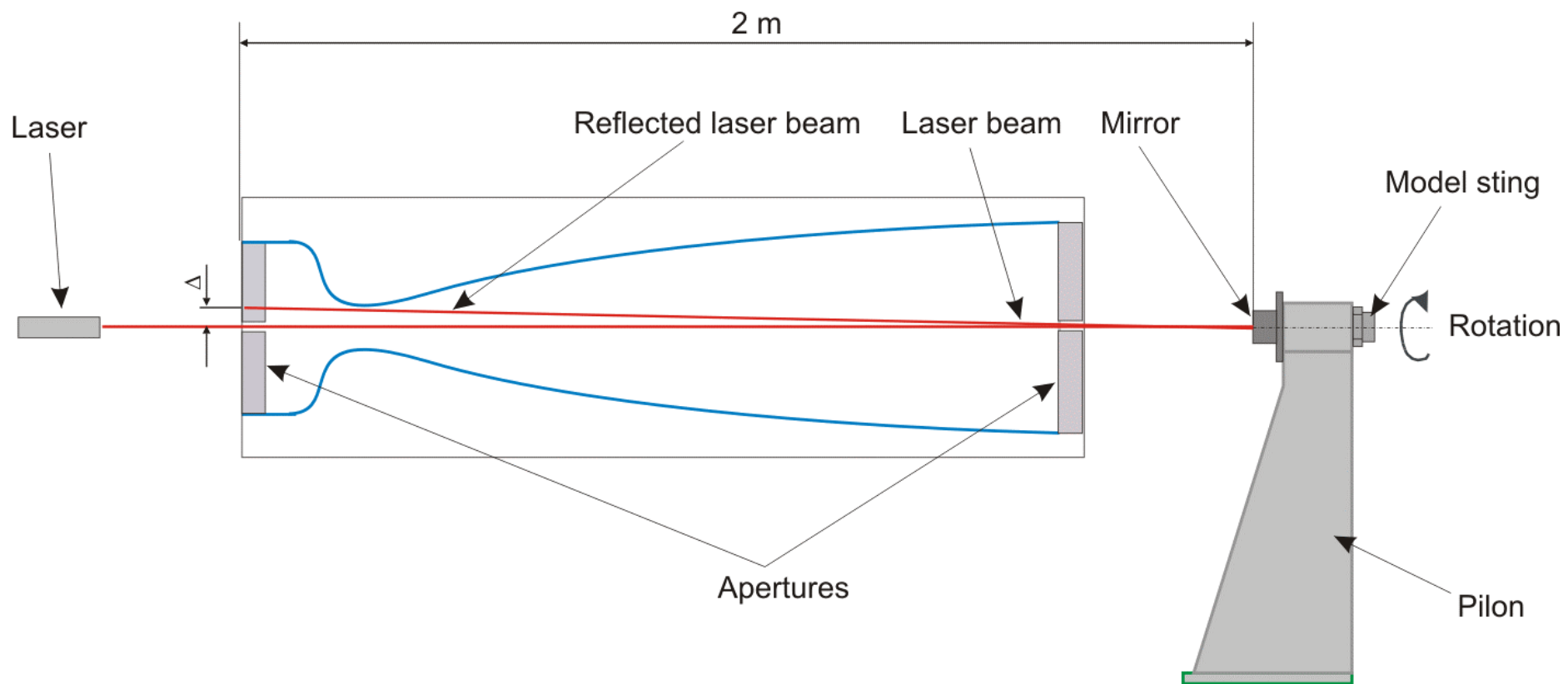
Fig. 7. Alignment at zero angles procedure.

Fig. 8. Model installed in test section of T-326.
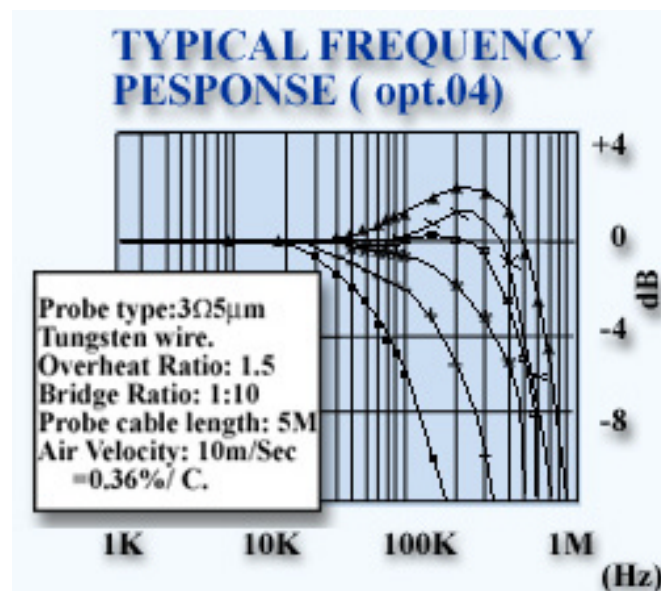
Fig. 9. The typical frequency response graph.

Data taken from AN-1003 Hot-Wire Anemometer with options 01 & 04. The amplitude is relative to the 1 kHz amplitude.
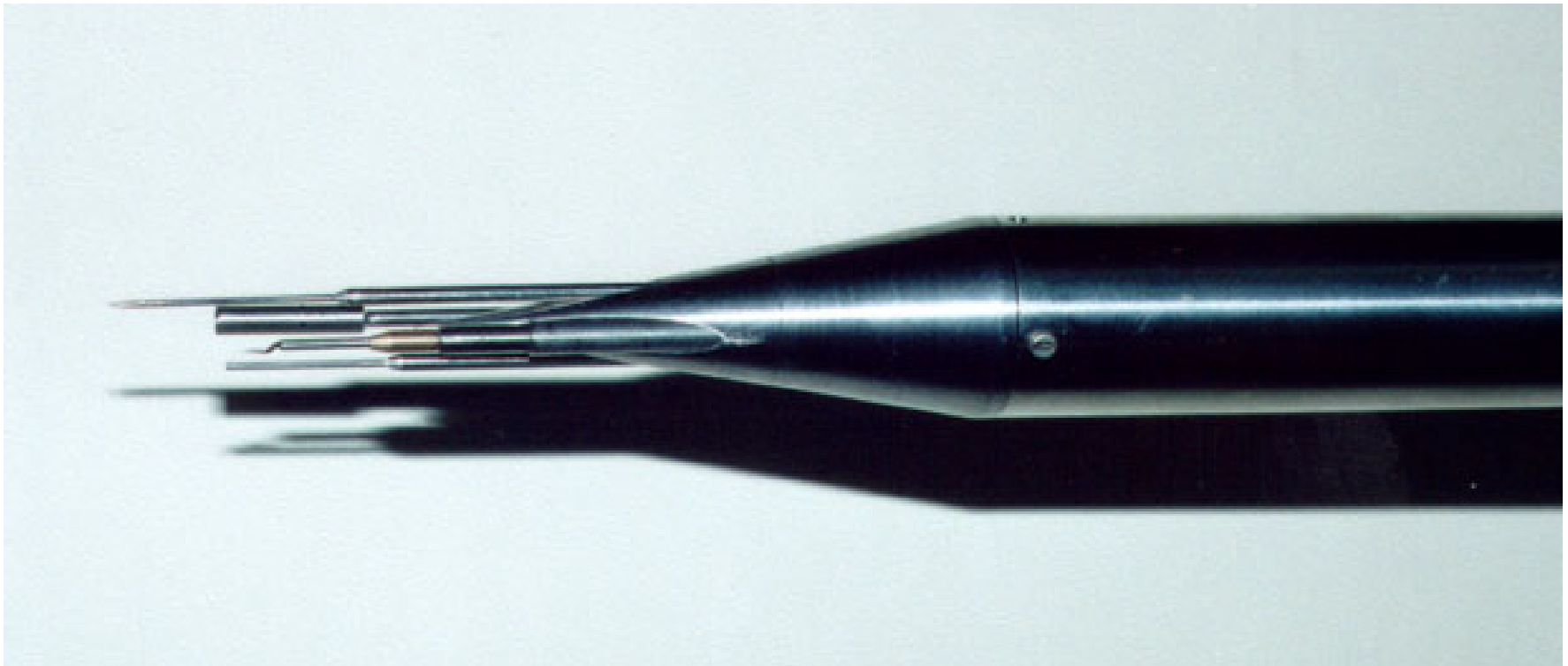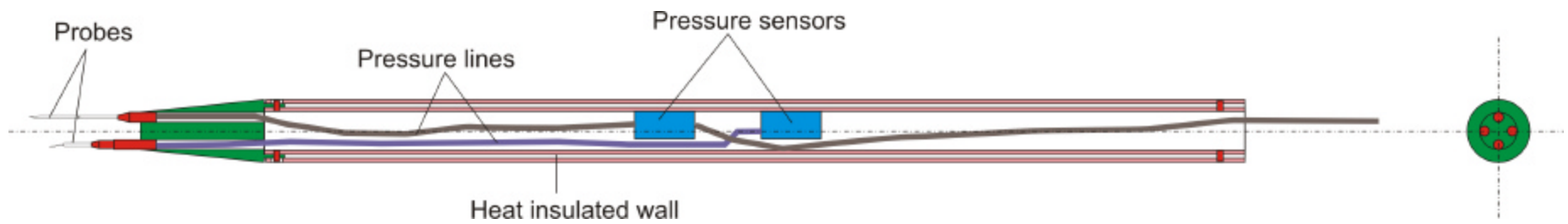
Fig. 10. Combined probe for free stream measurements.
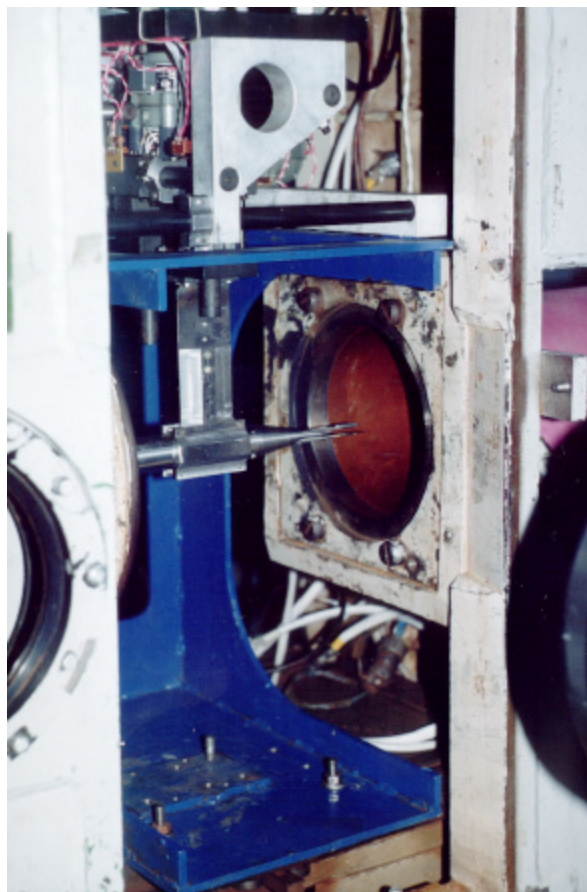
Fig. 11. Photo of combined probe installed on traversing system in test section.
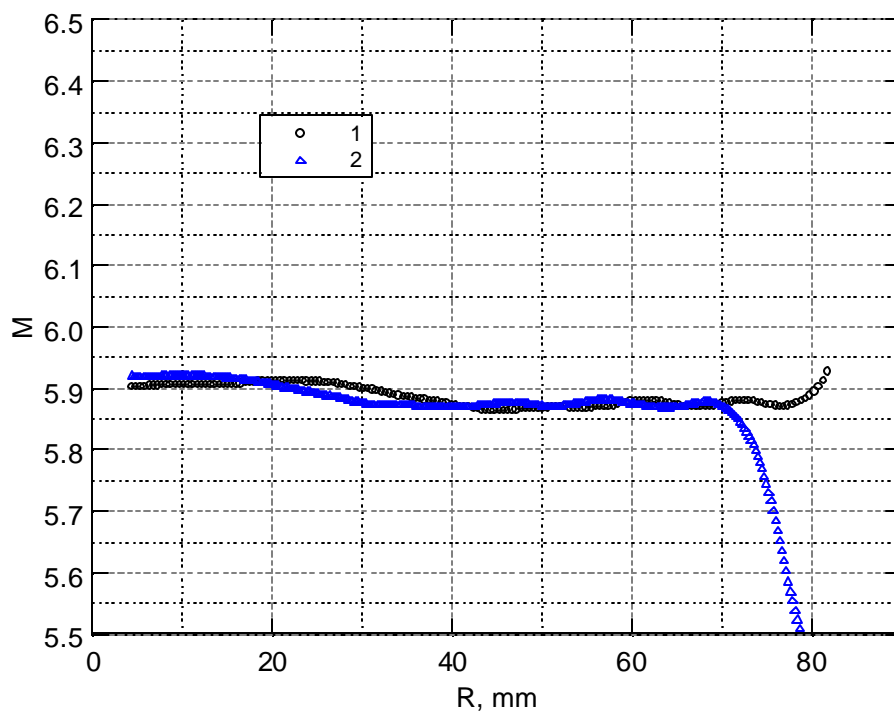
Fig. 12. Transverse Mach number distribution at nozzle exit. 1-P$_0$¢P$_0$; 2-P$_¥$/P$_0$.
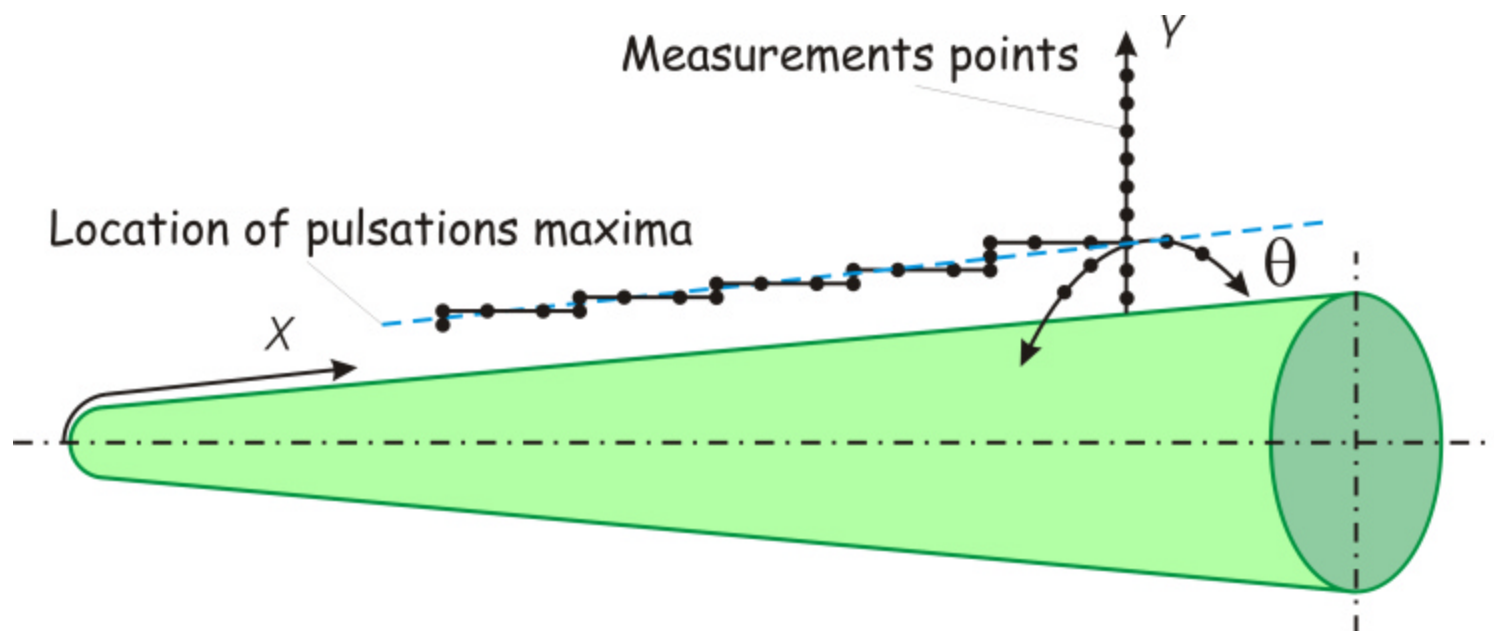
Fig. 13. Procedure of artificial disturbances measurement.
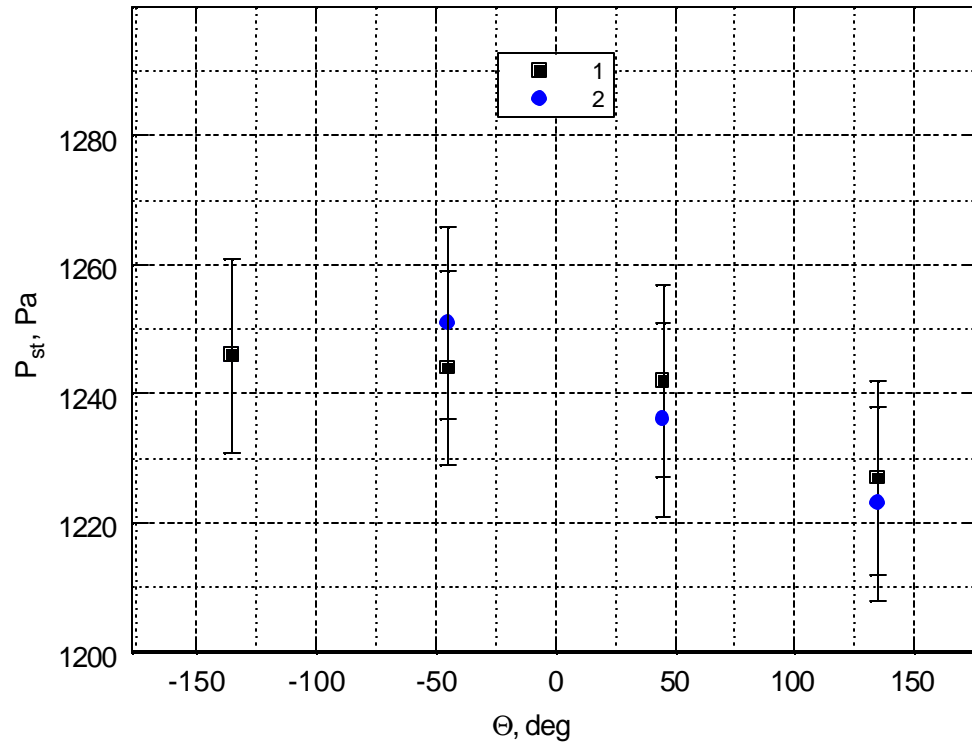
Fig. 14. Pressure distribution around model.
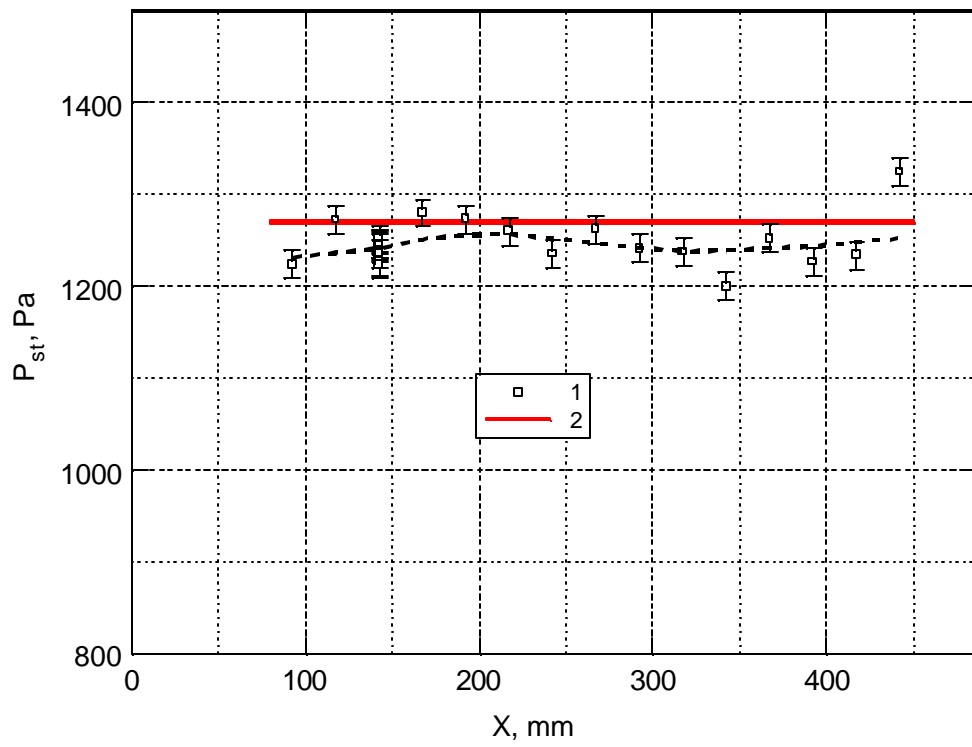
Fig. 15. Pressure distribution over the cone generatrix.
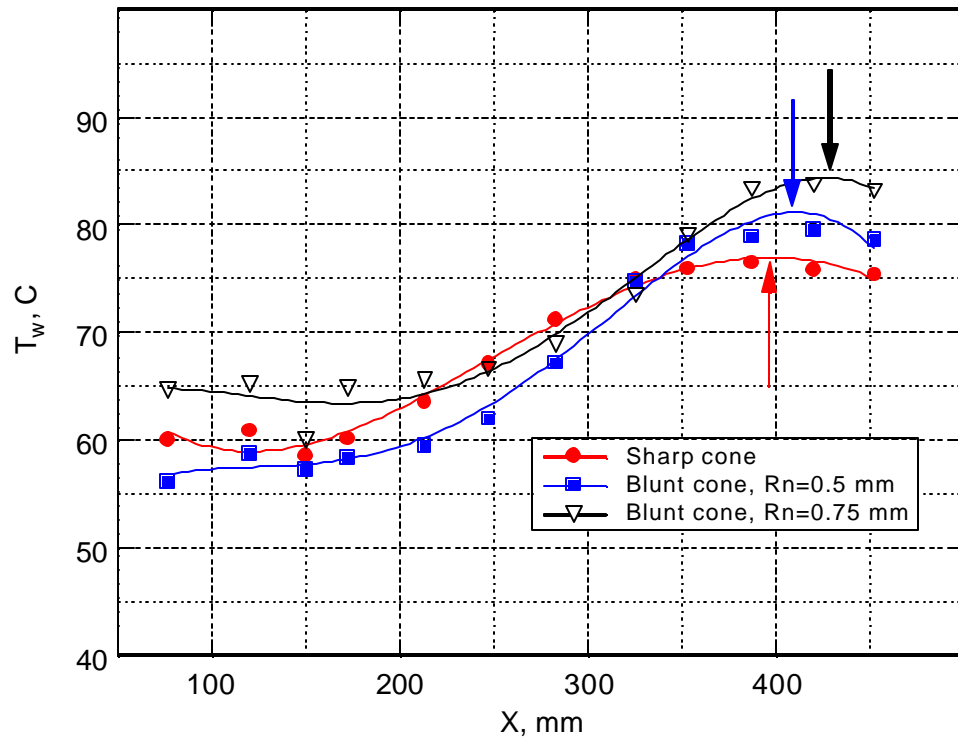
Fig. 16. Wall temperature distribution along model.
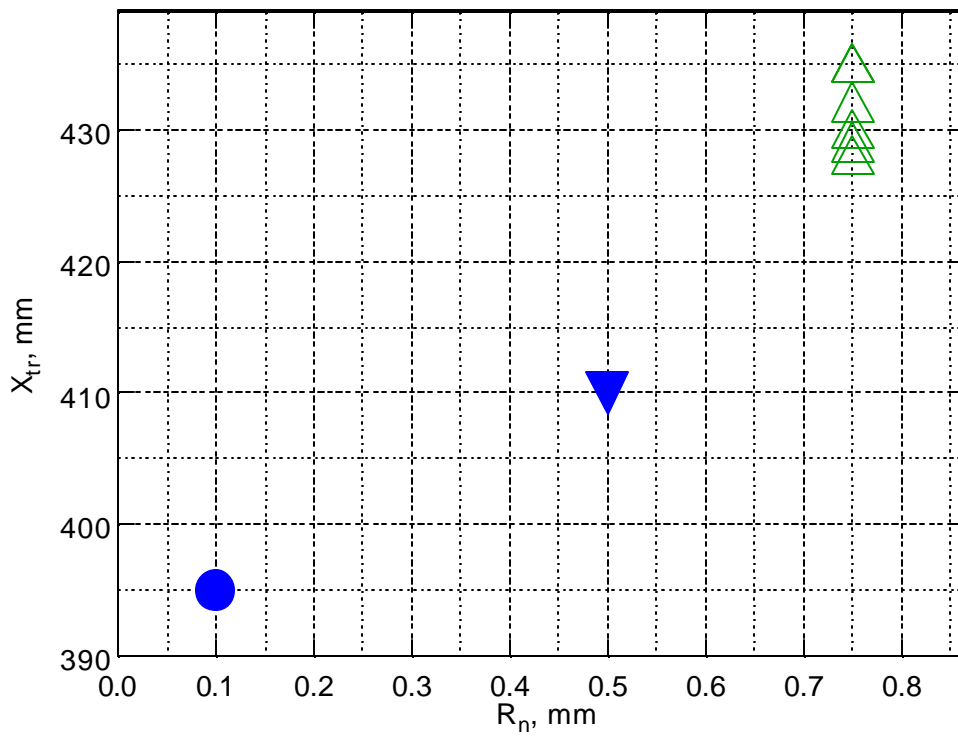
Fig. 17. Laminar-turbulent transition location versus R_n.
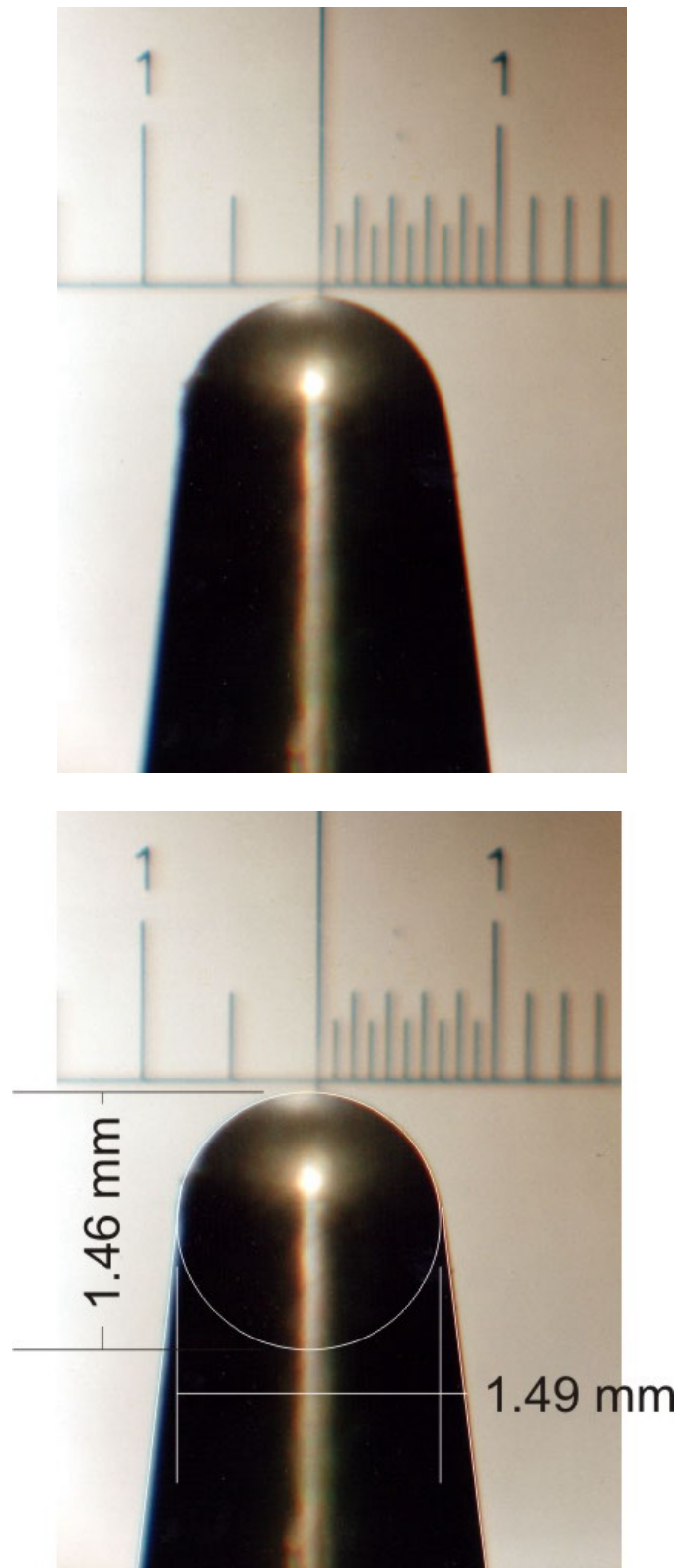
Fig. 18. Spherical bluntness.
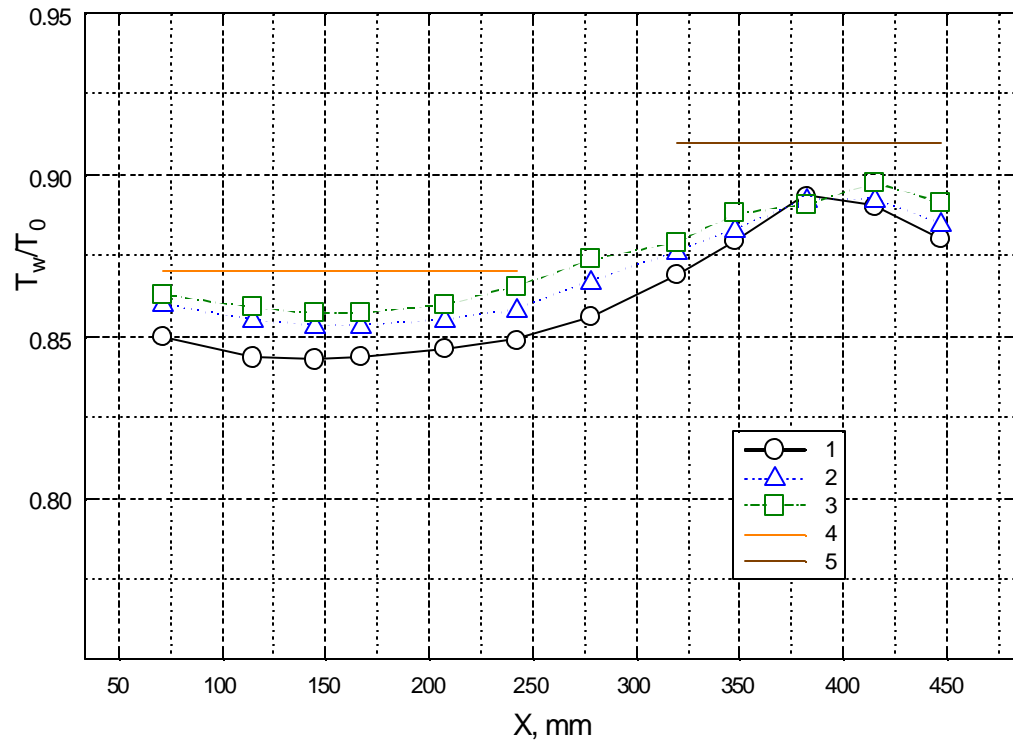
Fig. 19. Example of temperature factor T_w/T_0 distribution over the generatrix for one run.
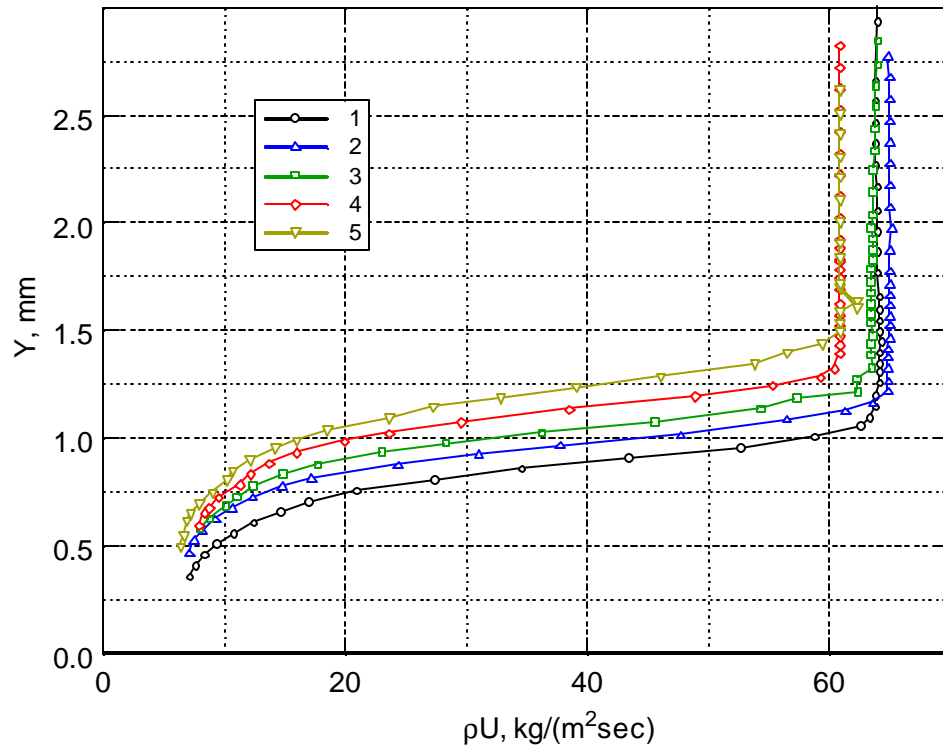
Symbols 1-5 correspond to X=107, 136, 166, 190, 227 mm.
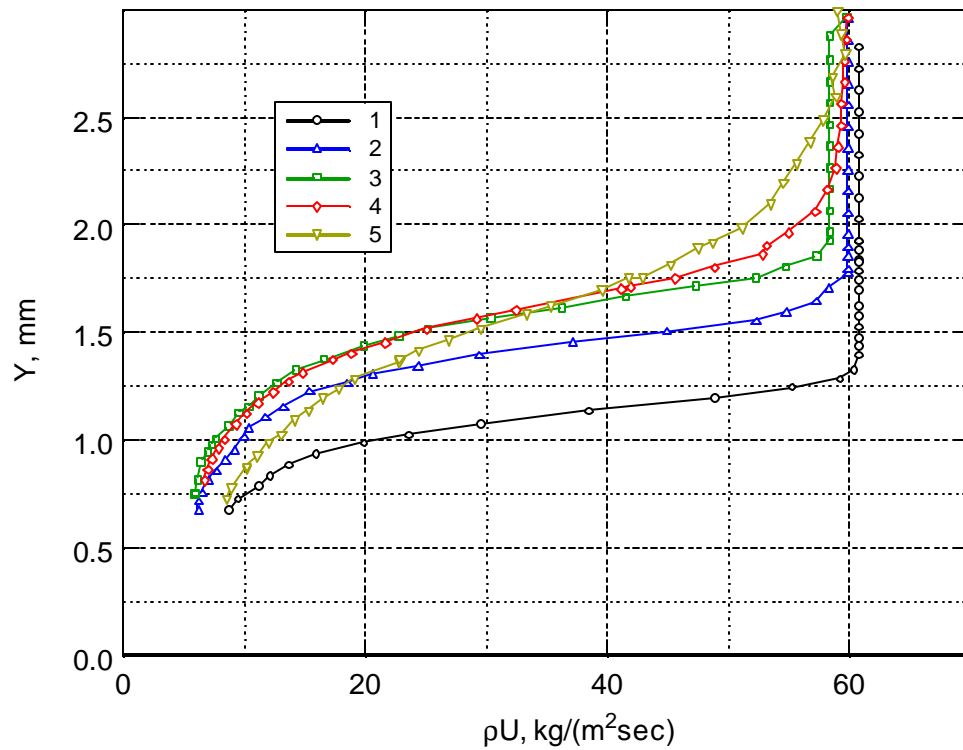
Symbols 1-5 correspond to X=257, 273, 304, 334, 365 ? ? .

Fig. 20. Mass flow distributions across boundary layer.
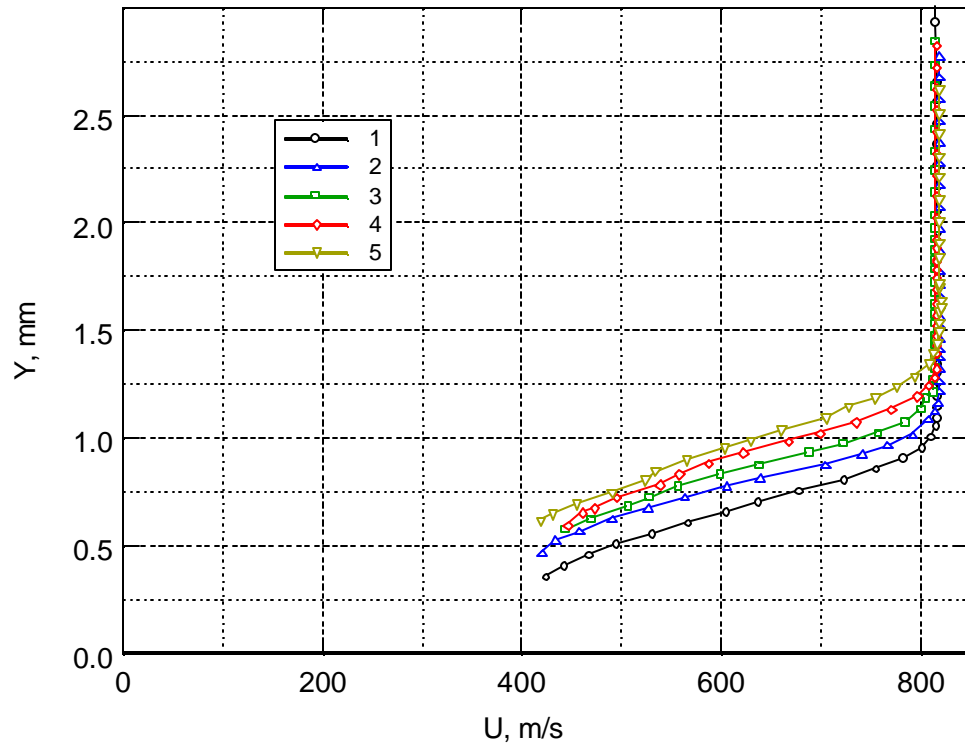
Symbols 1-5 correspond to *X*=107, 136, 166, 190, 227 mm.
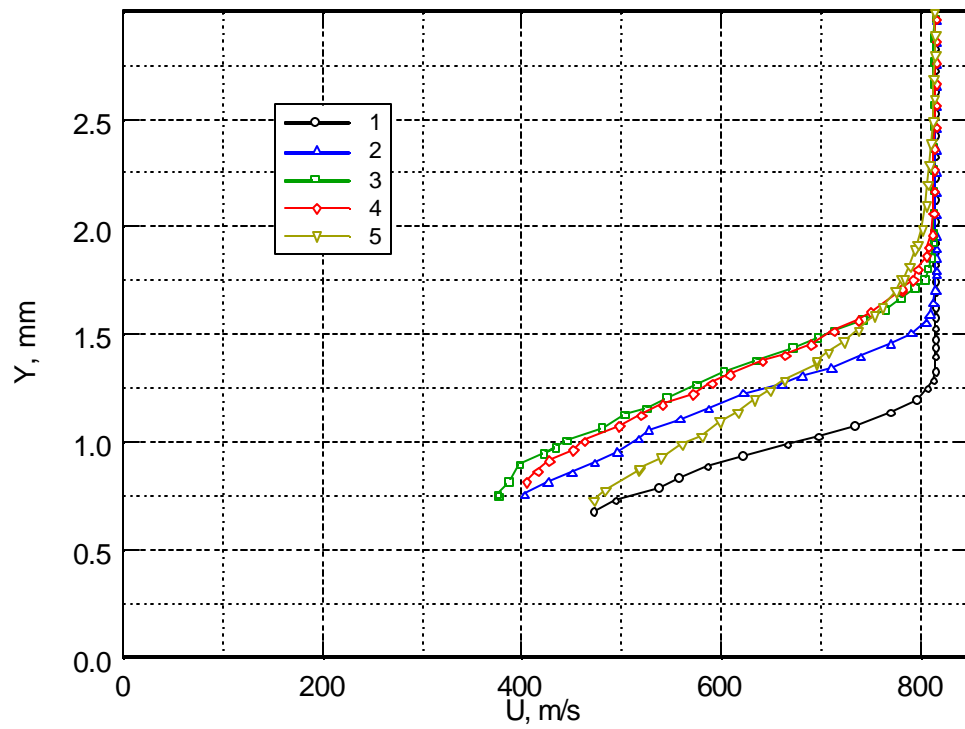
Symbols 1-5 correspond to *X*=257, 273, 304, 334, 365 ? ? .

Fig. 21. Velocity distributions across boundary layer.
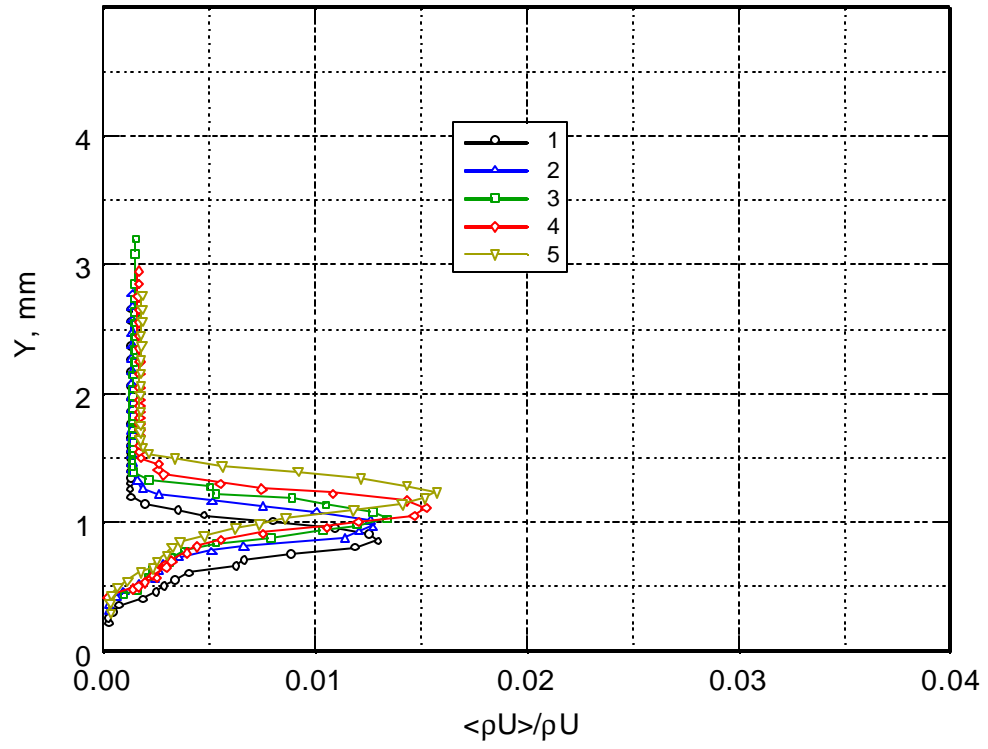
Symbols 1-5 correspond to *X*=107, 136, 166, 190, 227 mm.
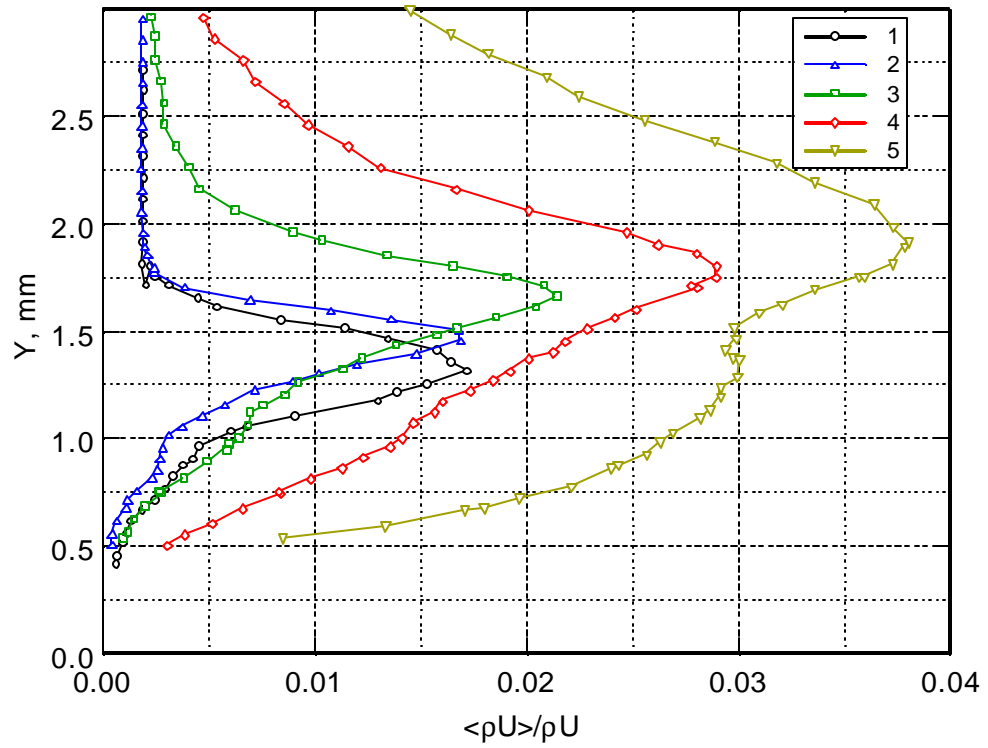
Symbols 1-5 correspond to *X*=257, 273, 304, 334, 365 ? ? .

Fig. 22. Distributions integral RMS mass flow pulsations across boundary layer.
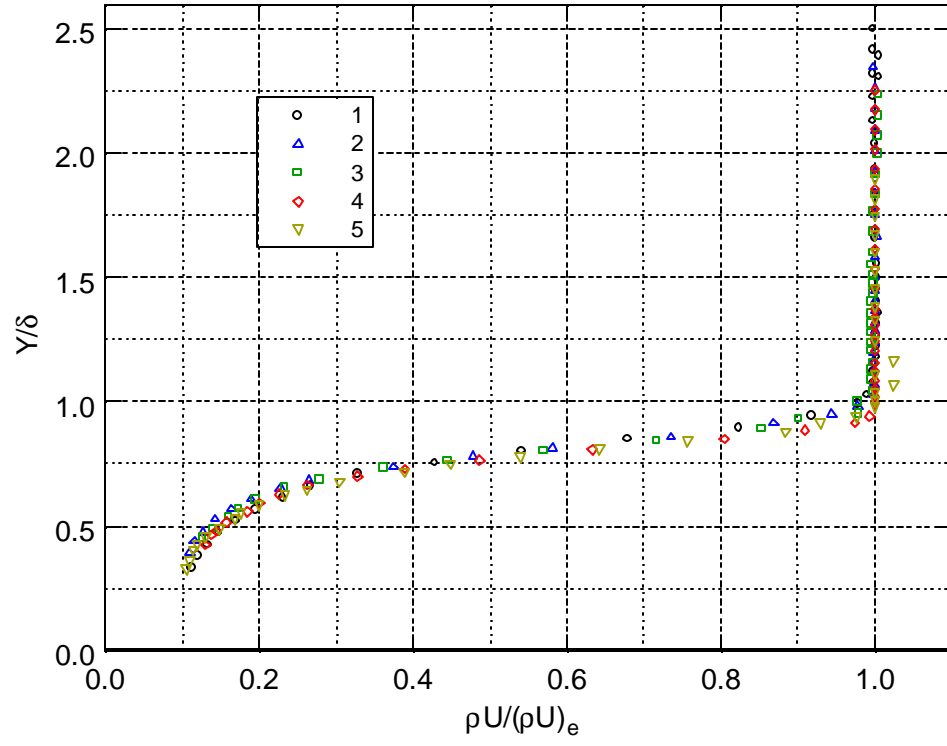
Symbols 1-5 correspond to $X=107, 136, 166, 190, 227$ mm.
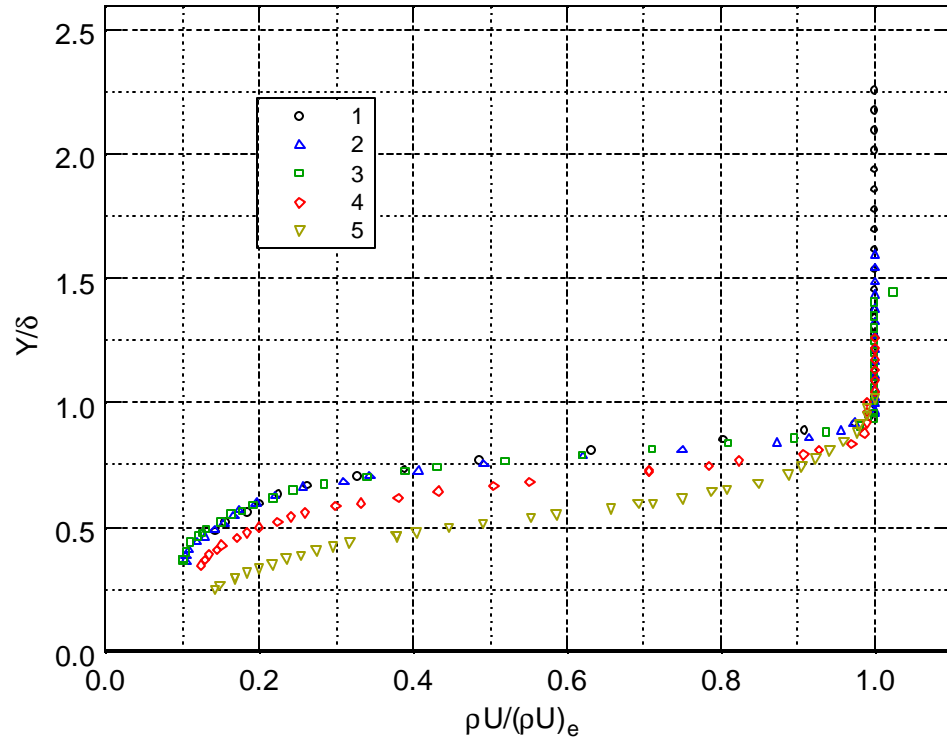
Symbols 1-5 correspond to $X=257, 273, 304, 334, 365$? ? .

Fig. 23. Normalized mass flow distributions across boundary layer.
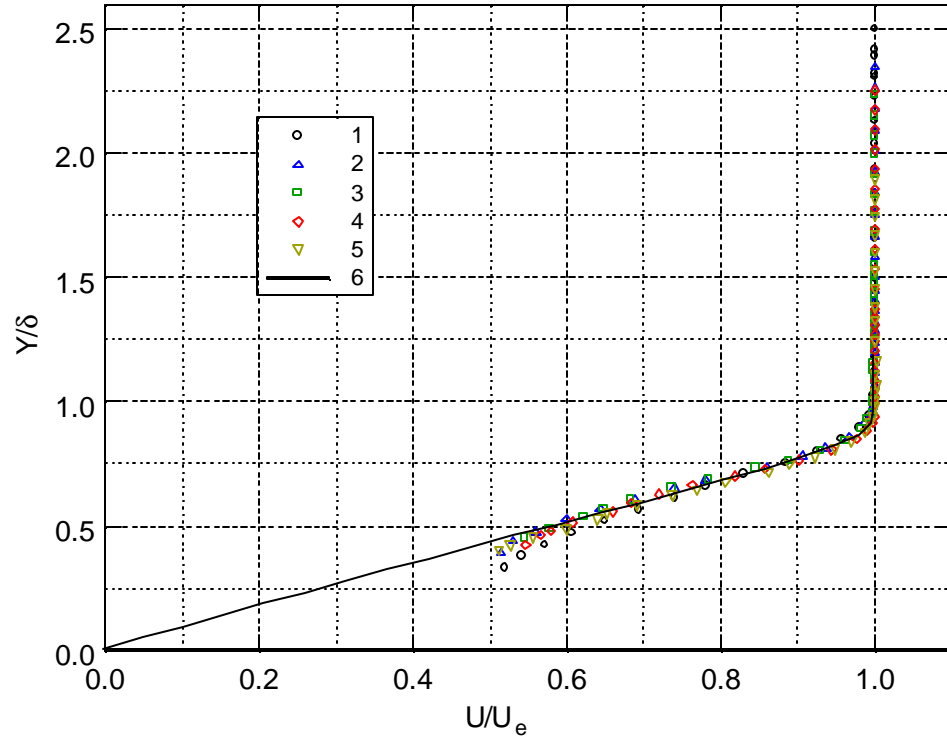
Symbols 1-5 correspond to *X*=107, 136, 166, 190, 227 mm.
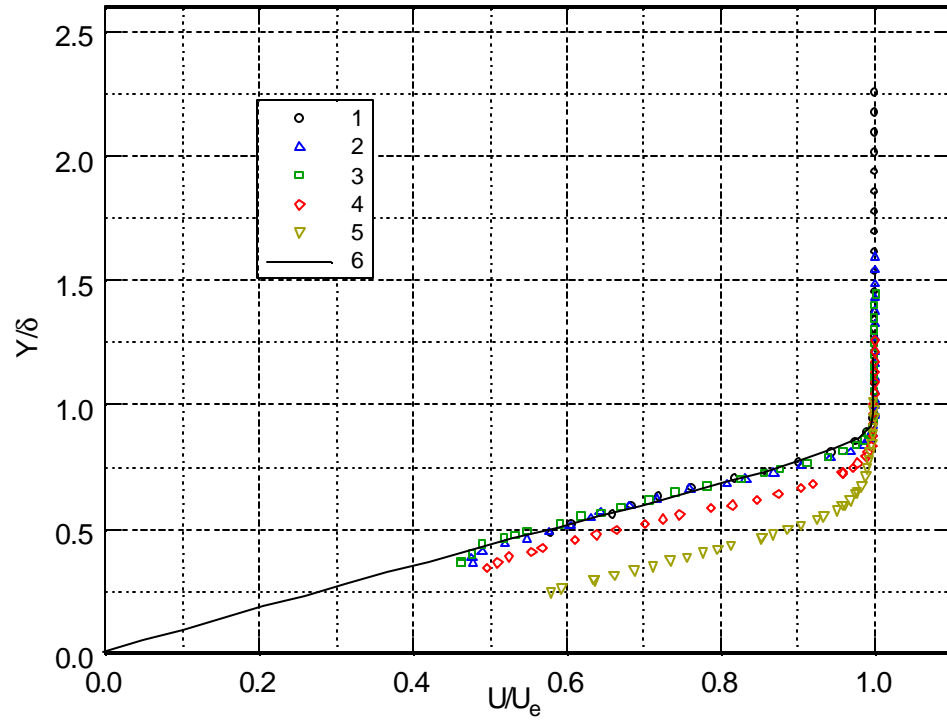
Symbols 1-5 correspond to *X*=257, 273, 304, 334, 365 ? ? .

Fig. 24. Normalized velocity distributions across boundary layer.
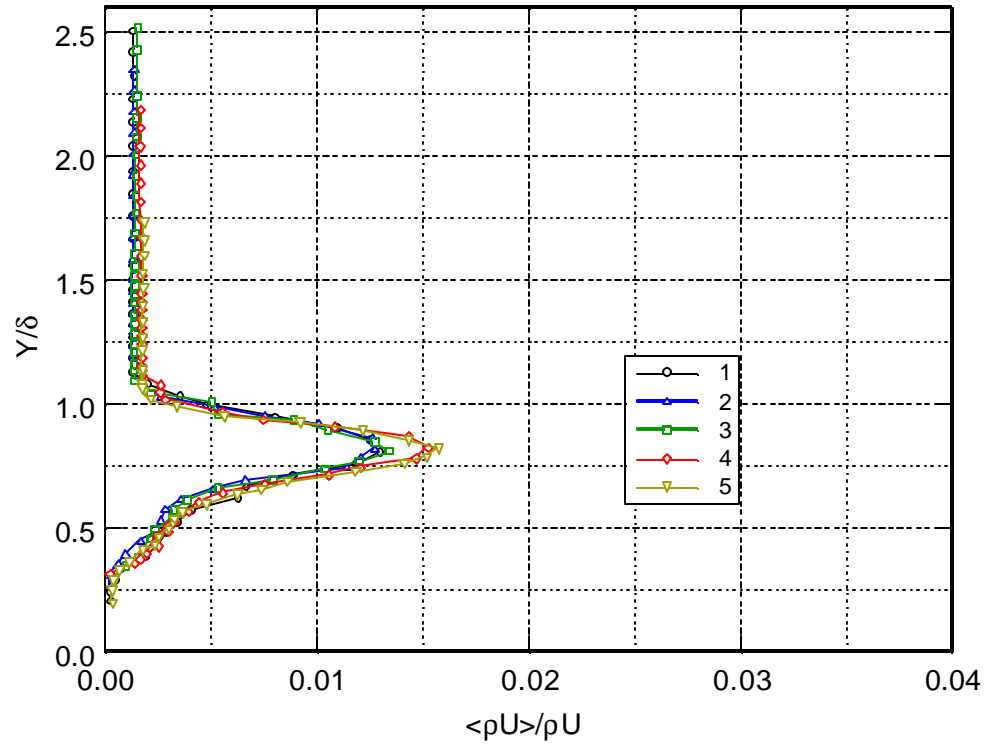
Symbols 1-5 correspond to *X*=107, 136, 166, 190, 227 mm.
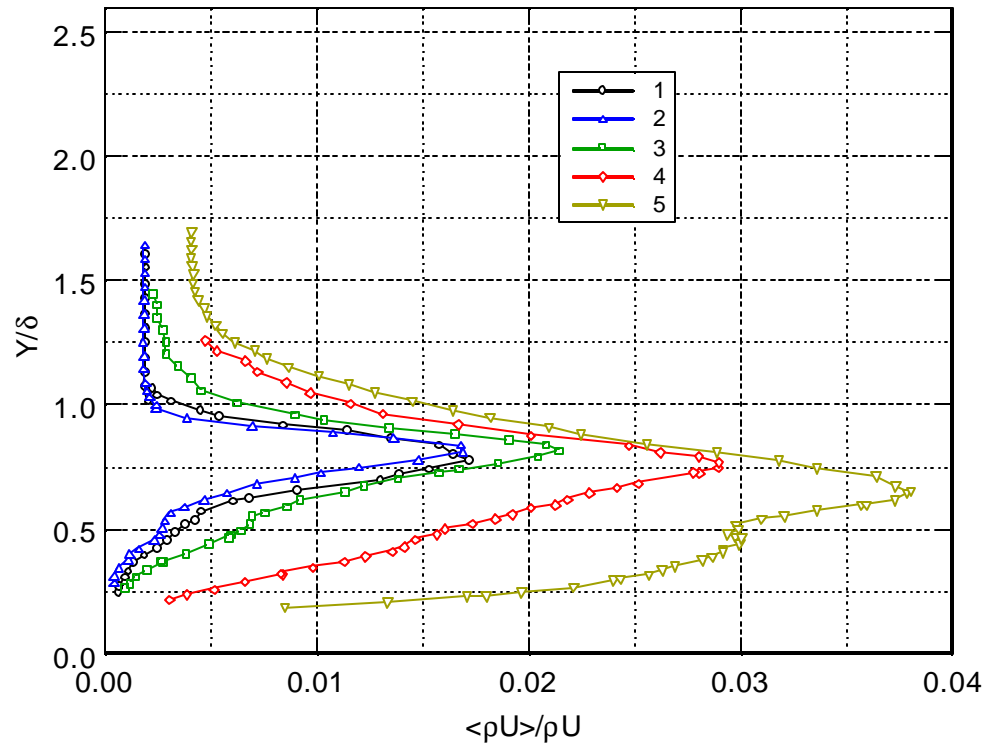
Symbols 1-5 correspond to *X*=257, 273, 304, 334, 365 ? ? .

Fig. 25. Normalized distributions integral RMS mass flow pulsations across boundary layer.

53
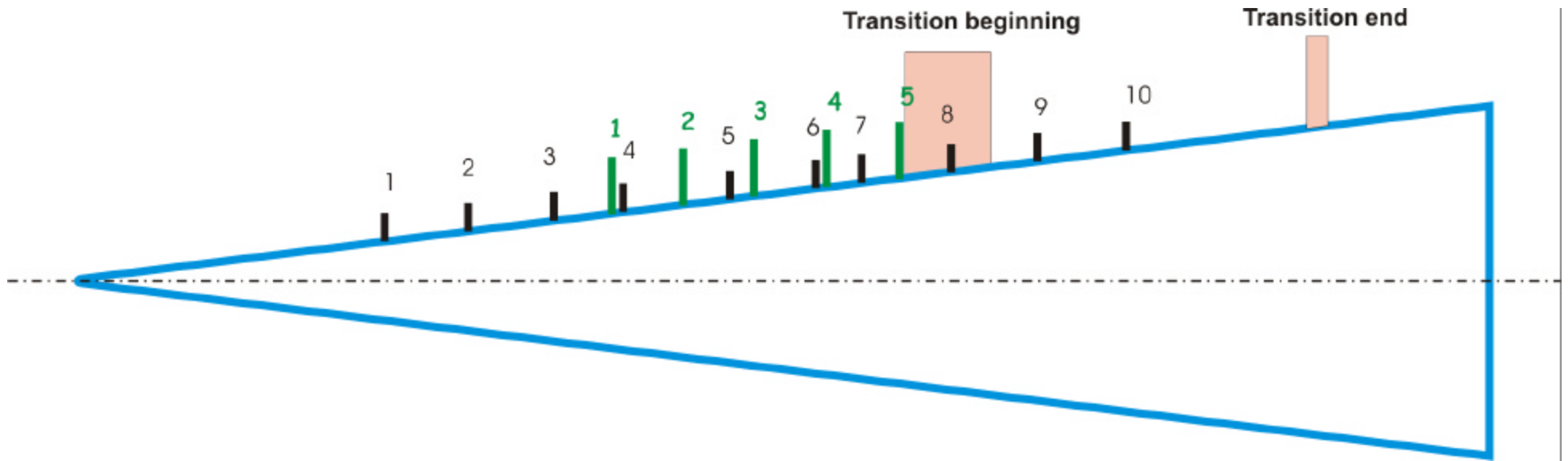
Fig. 26. Locations of measurement cross sections.

Black lines corresponds to measurements with CTA, green lines – CCA.
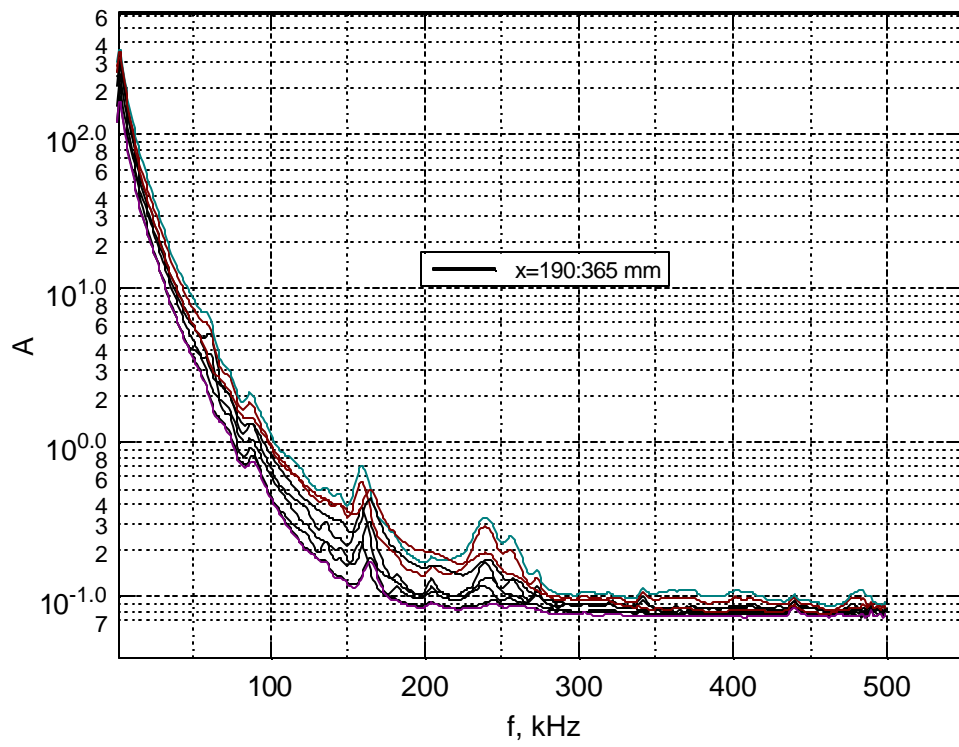
Fig. 27. Spectra of mass flow pulsations in the layer of maximum pulsations.
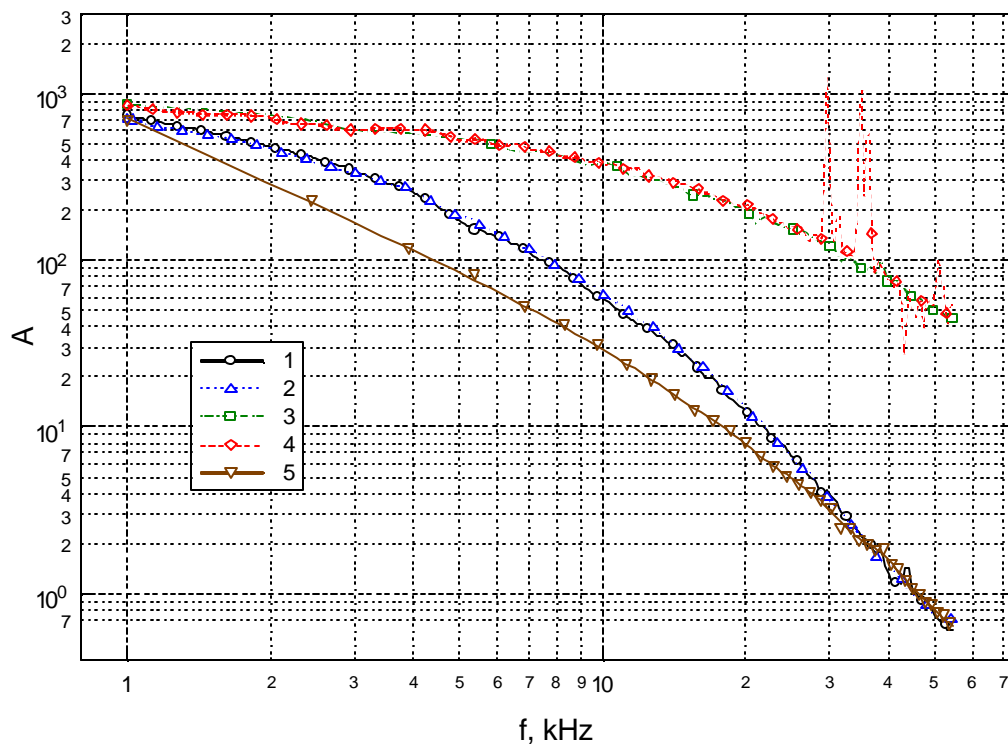
Fig. 28. Comparison of spectra for CTA and CCA.

CTA (1 – AN-1003, 2 – ITAM CTA); CCA (3 – ITAM CCA, 4 – CCA built by the authors), uncompensated signal of hot-wire, CCA bridge (5).
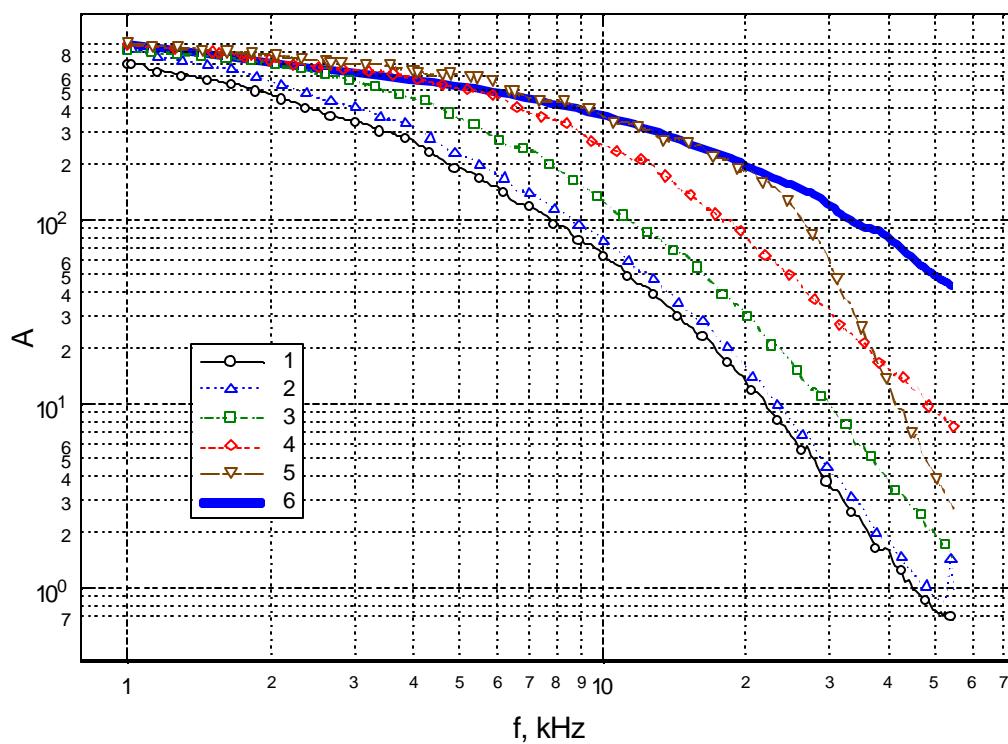
Fig. 29. Spectra for AN-1003 at different adjustment of frequency compensation circuit.

1-5 – frequency range of CTA decreases. 6 – spectrum of CCA.
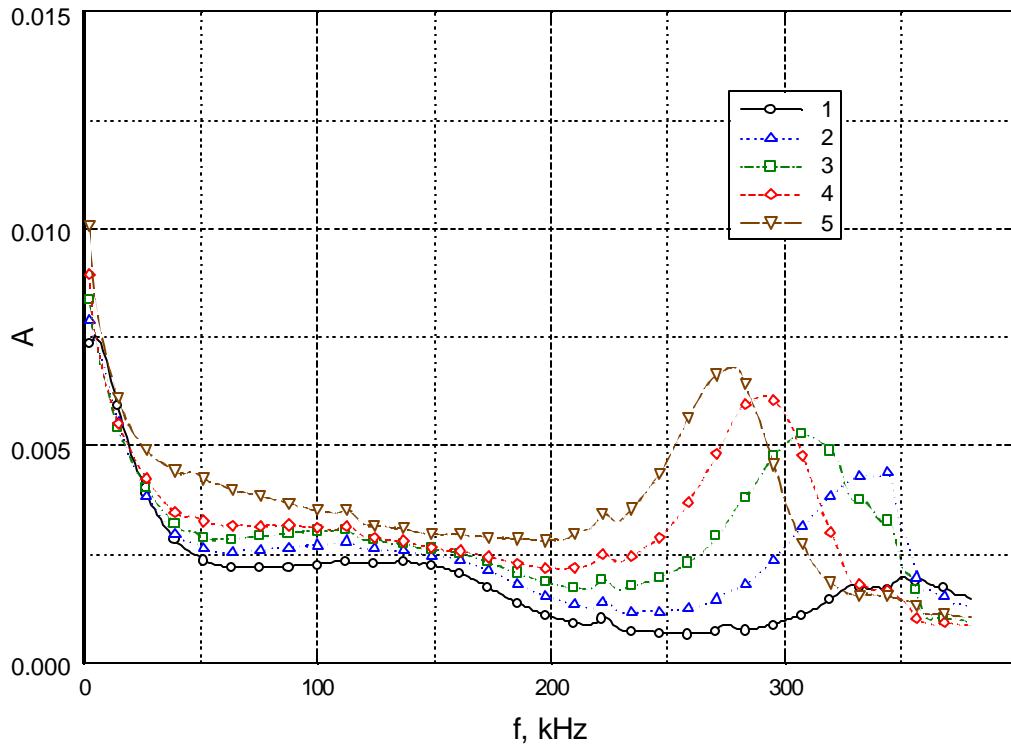
Fig. 30. Spectra obtained with new CCA for sharp cone.

Symbols 1-5 correspond to X=192.8, 217.8, 242.9, 268.0, 293.0 mm.
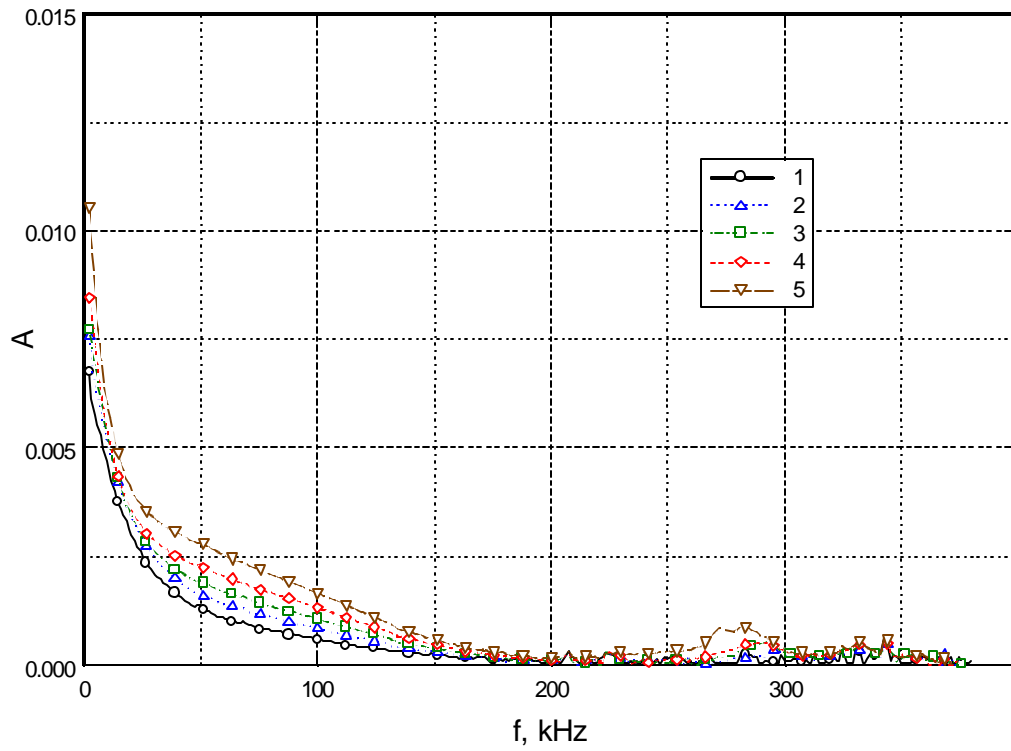
Fig. 31. Spectra obtained with new CCA for blunt cone.

Symbols 1-5 correspond to X=186.0, 210.3, 235.5, 260.8, 286.0 mm.

57
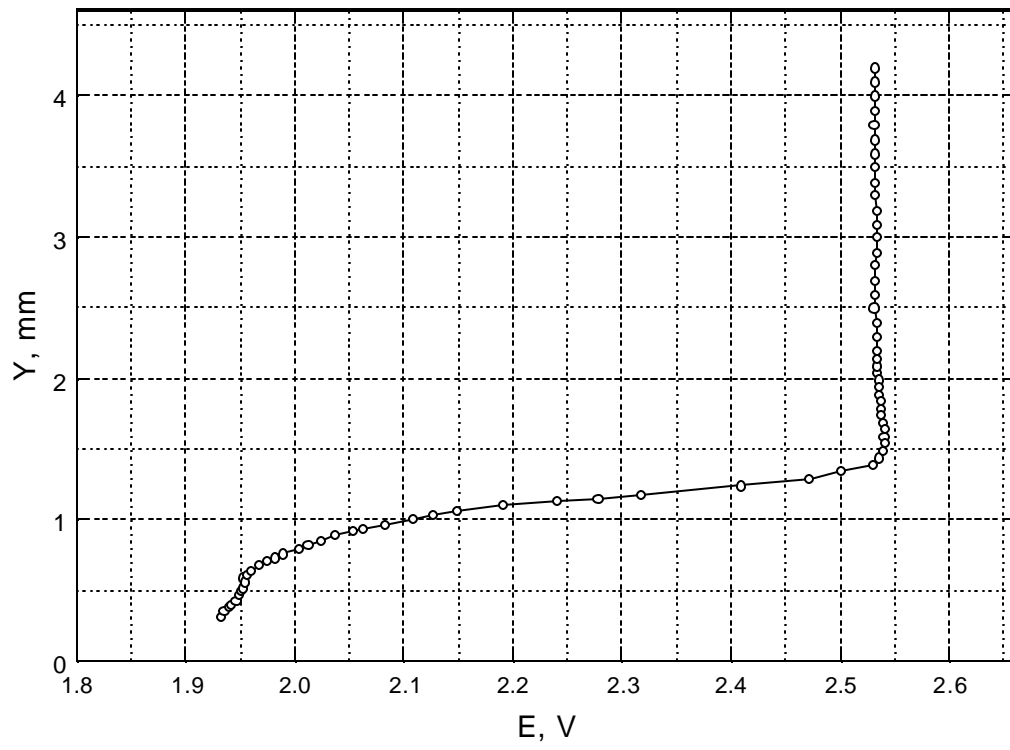
Fig. 32. Vertical distribution of mean voltage.
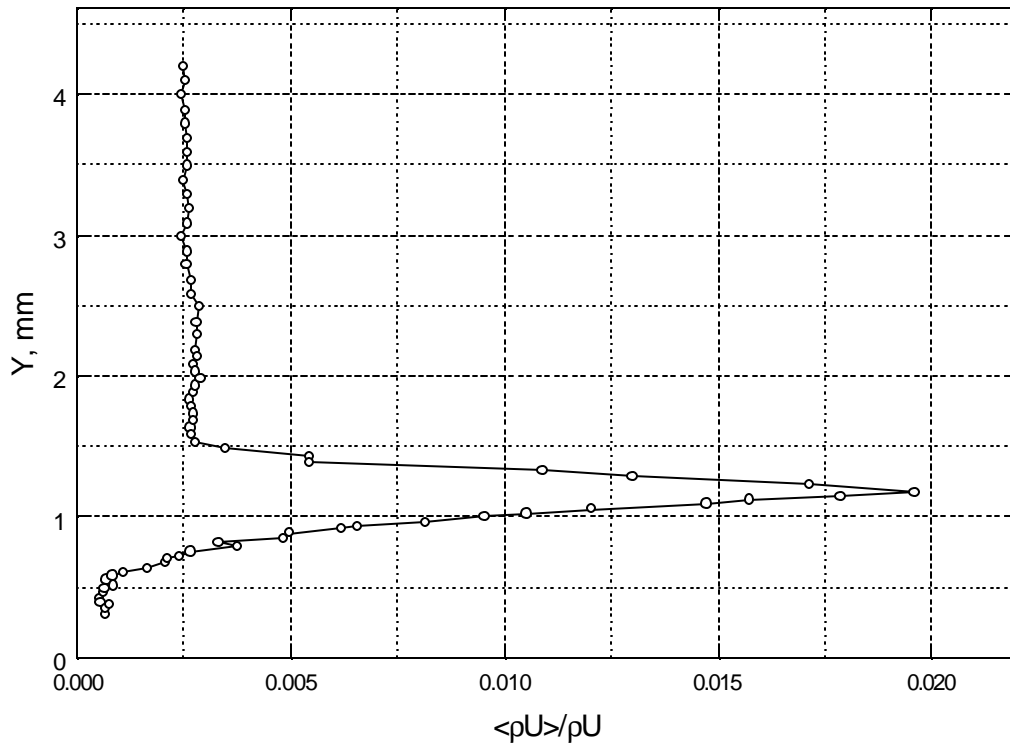
Fig. 33. Vertical distribution of $<rU>$.
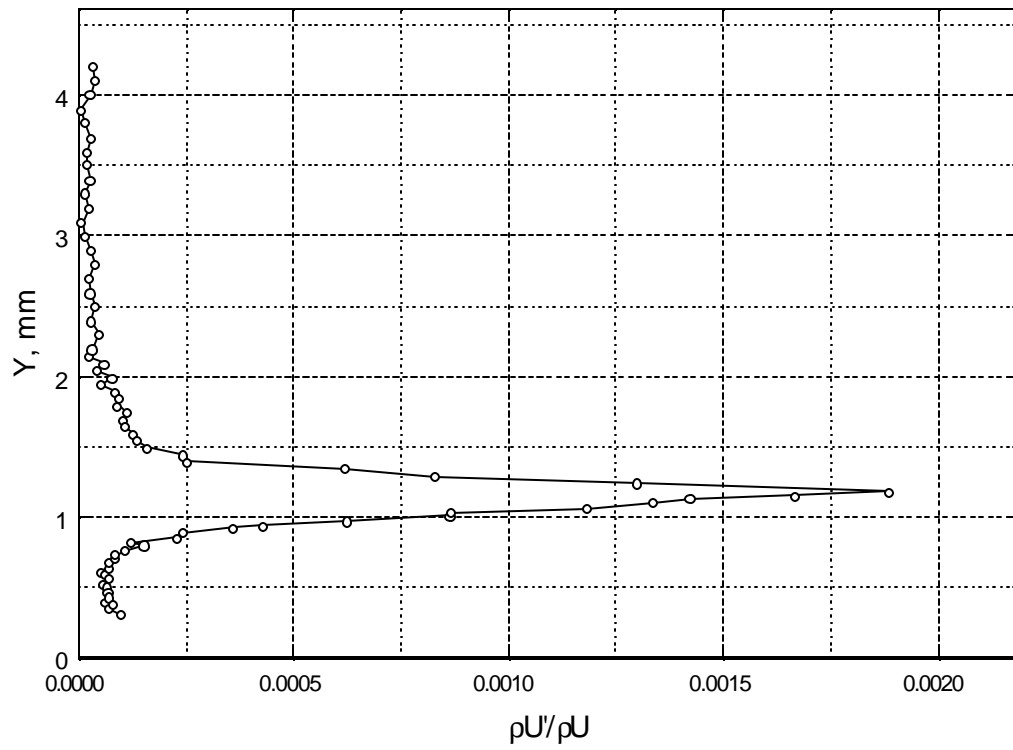
Fig. 34. Vertical distribution of amplitude in the center of wave packet.
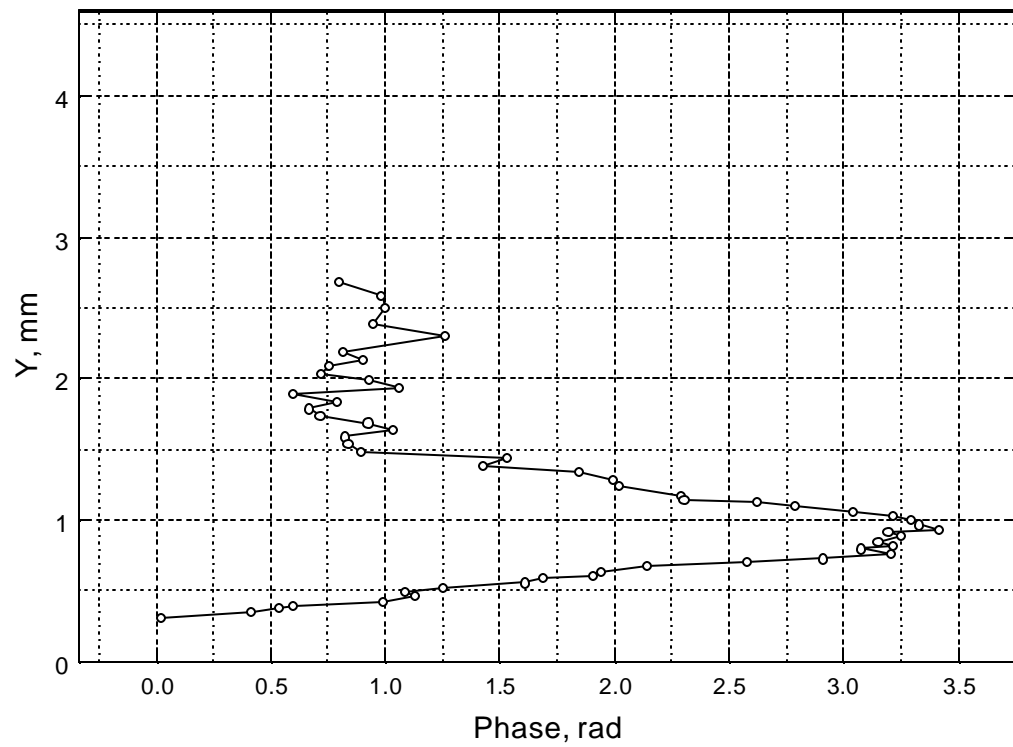
Fig. 35. Vertical distribution of phase in the center of wave packet.

59
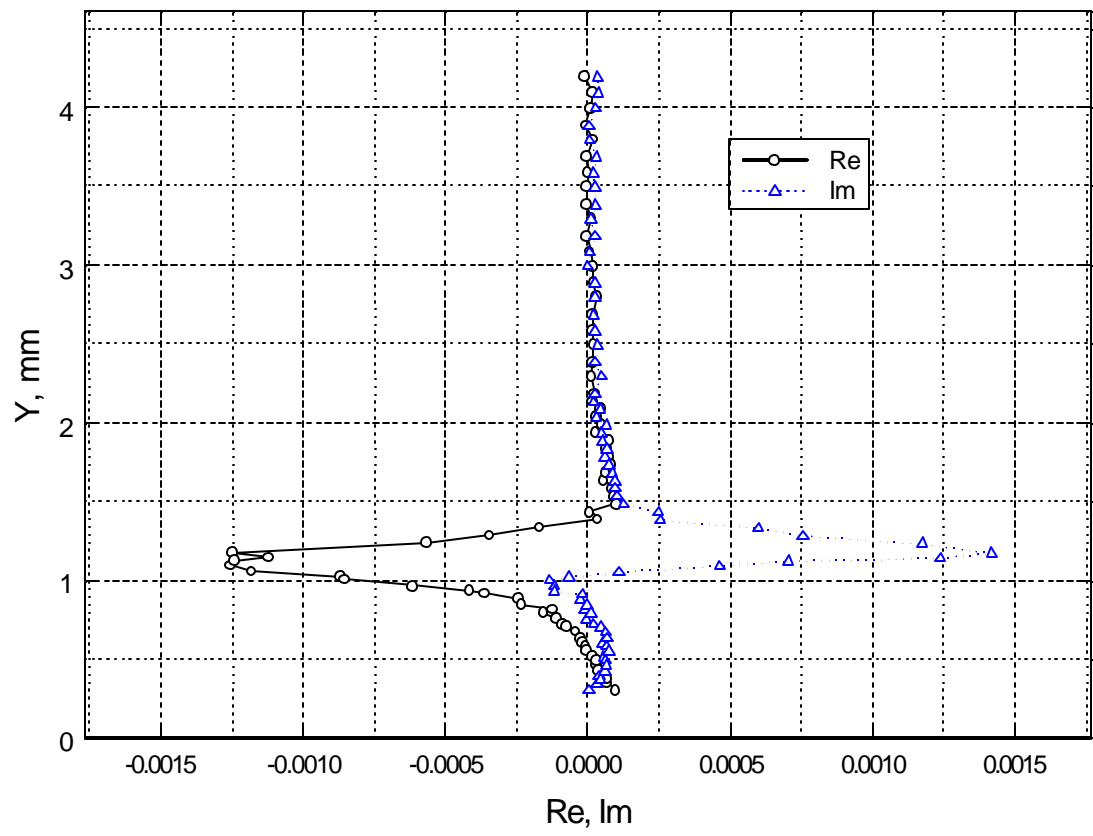
Fig. 36. Vertical distribution of Real and Imaginary parts in the center of wave packet.
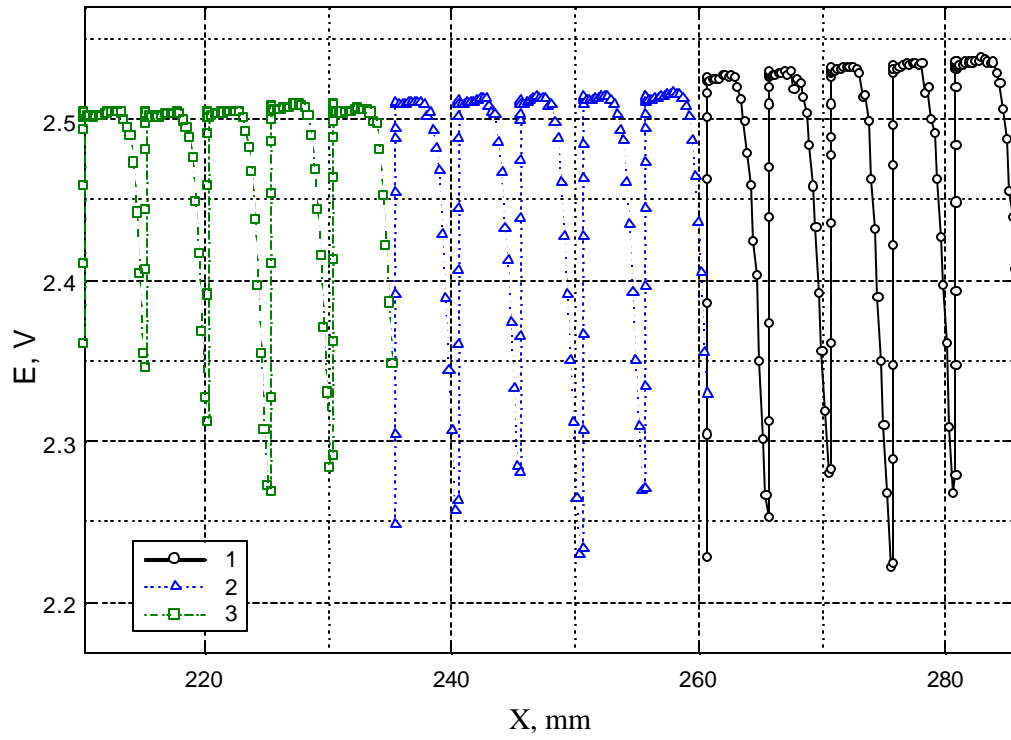
Fig. 37. Dependence of mean voltage on *X* for step measurements.
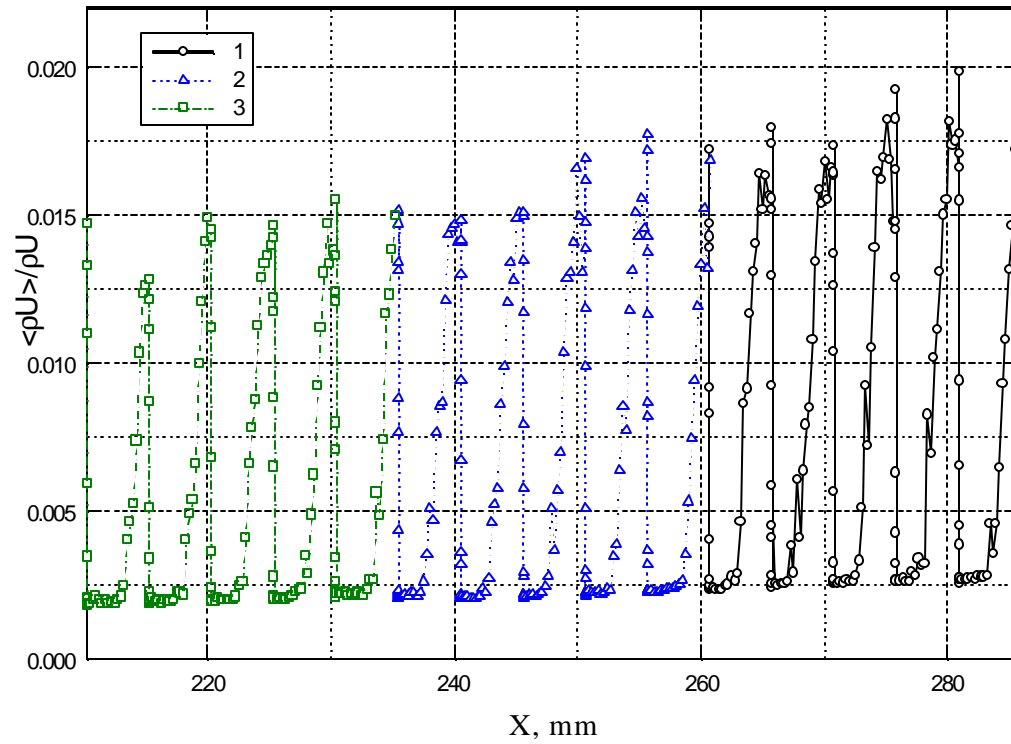
Fig. 38. Dependence of $<rU>$ on X for step measurements..
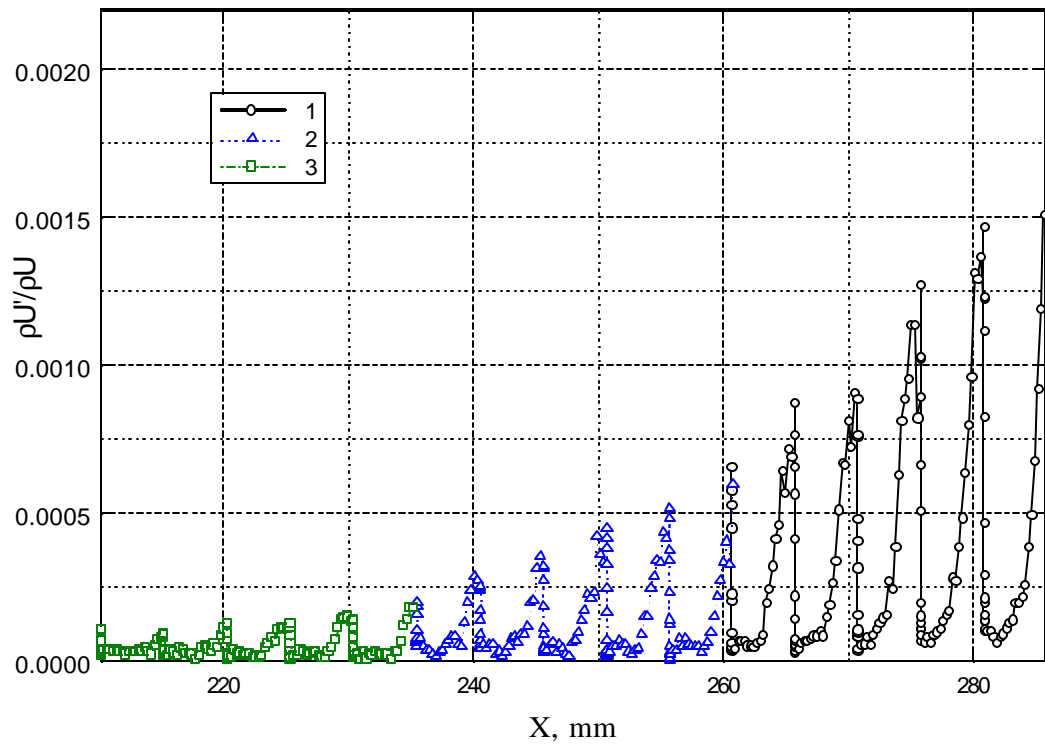
Fig. 39. Dependence of amplitude on X for step measurements.
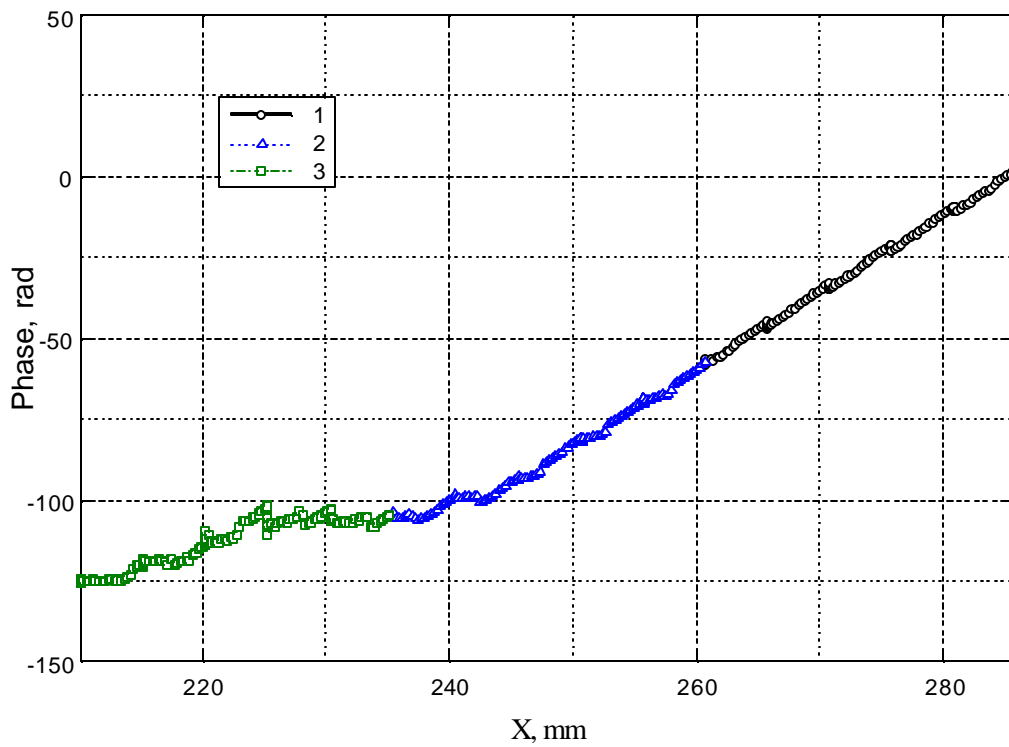
Fig. 40. Dependence of phase on *X* for step measurements.
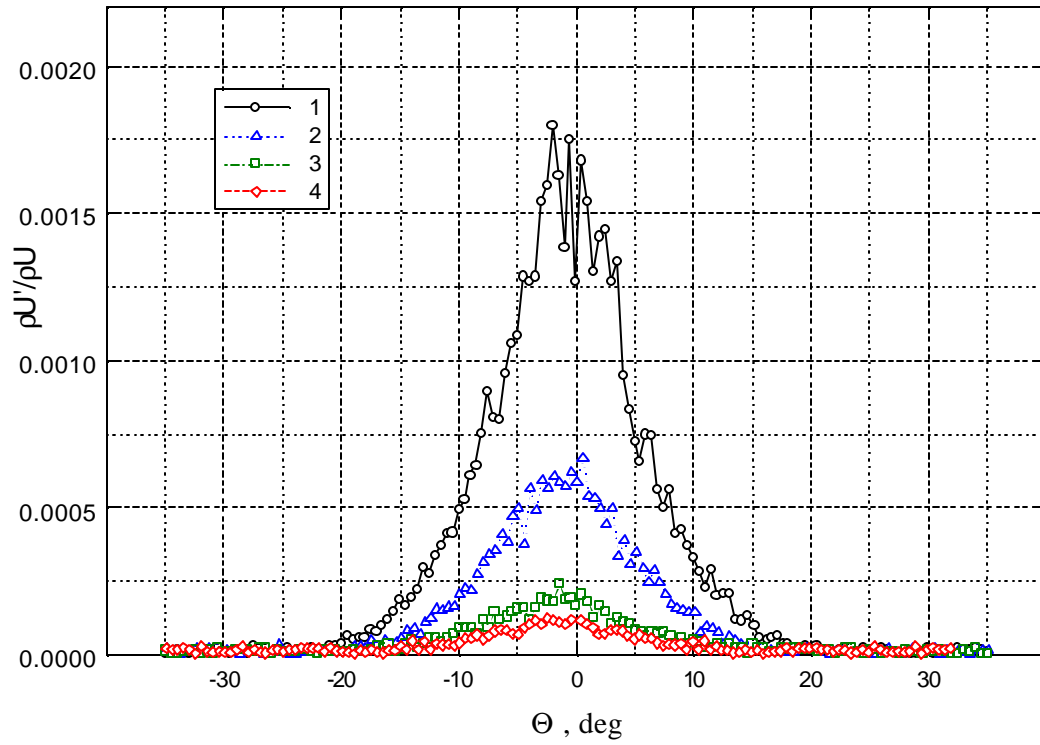
Fig. 41. Transversal distributions of amplitude in artificial wave packet.

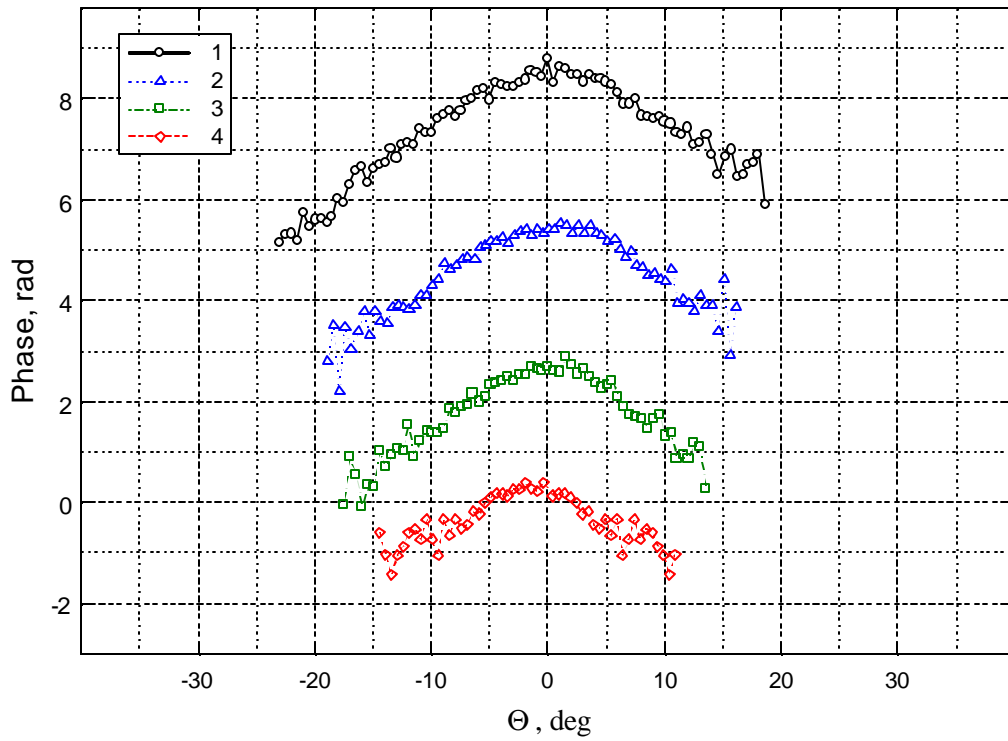Symbols 1-5 correspond to *X*=186.0, 210.3, 235.5, 260.8, 286.0 mm.

Fig. 42. Transversal distributions of phase in artificial wave packet.

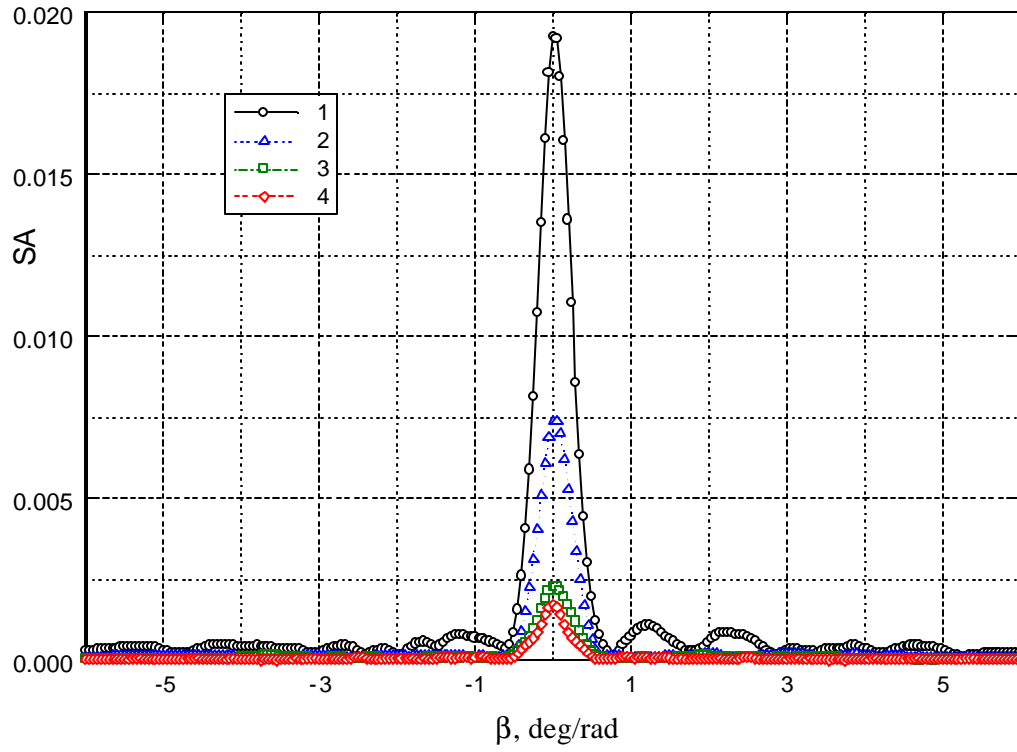Symbols 1-5 correspond to X=186.0, 210.3, 235.5, 260.8, 286.0 mm.

Fig. 43. Amplitude wave spectra with respect to the transversal wave number b.

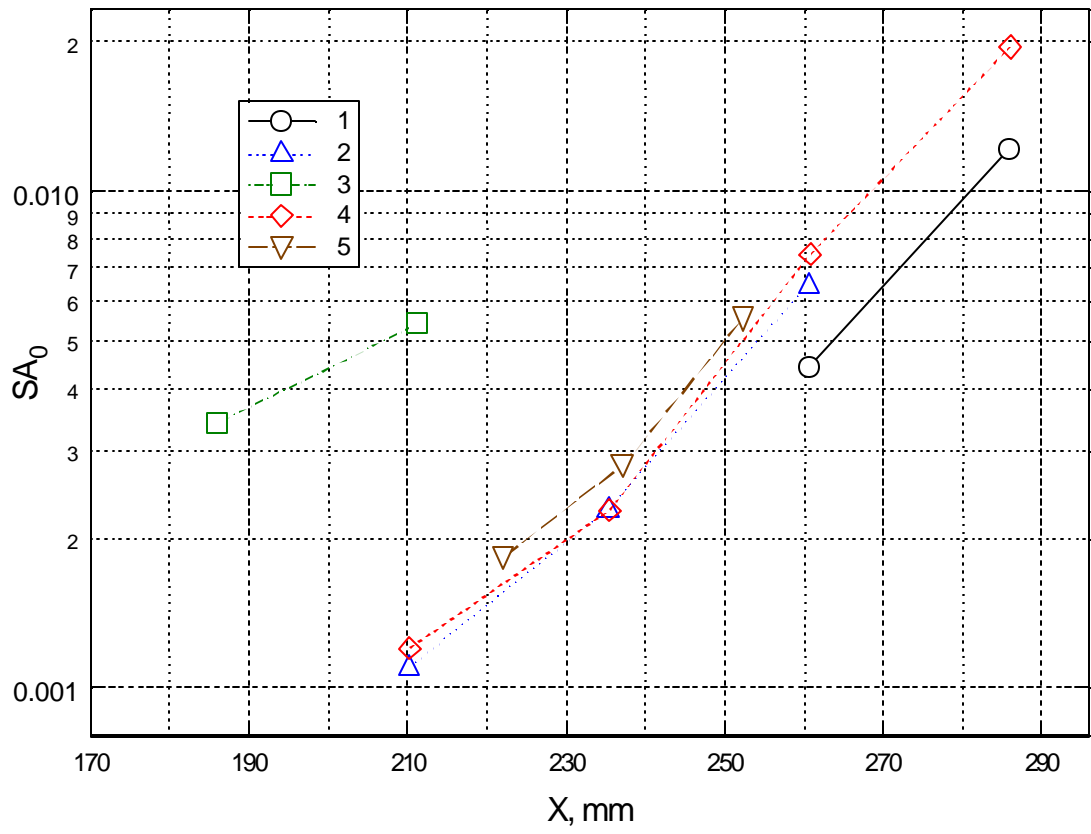Symbols 1-5 correspond to X=186.0, 210.3, 235.5, 260.8, 286.0 mm.

Fig. 44. Longitudinal distributions of wave amplitude for b=0 for 5 runs.
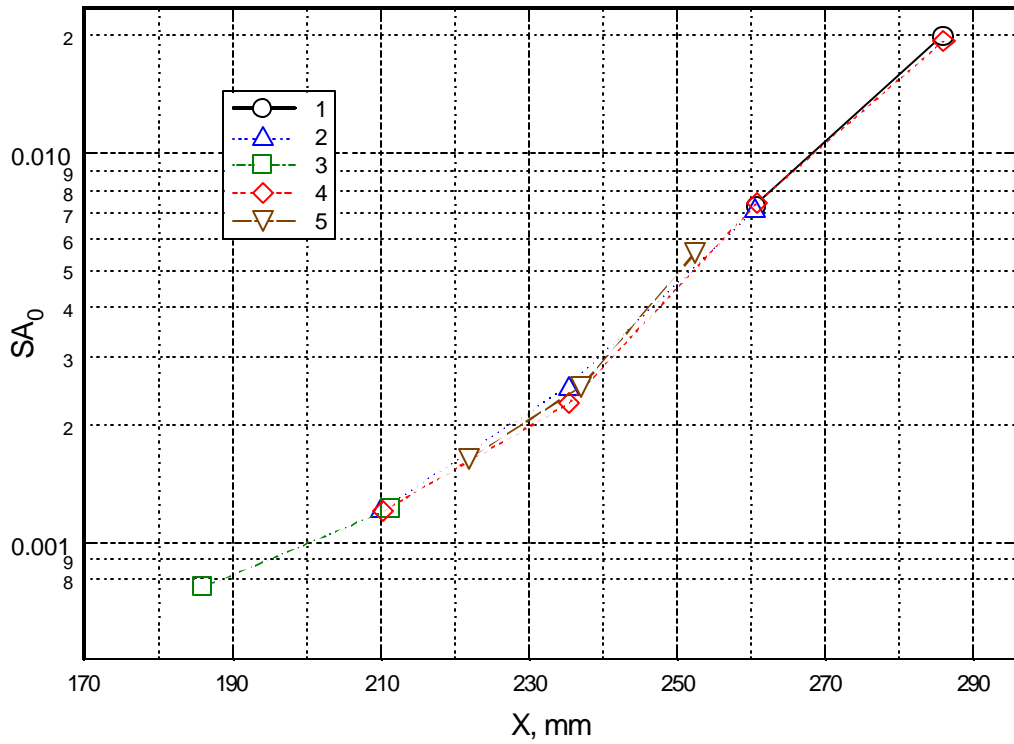

Fig. 45. Normalized longitudinal distributions of wave amplitude for b=0 for 5 runs in logarithmic scale.
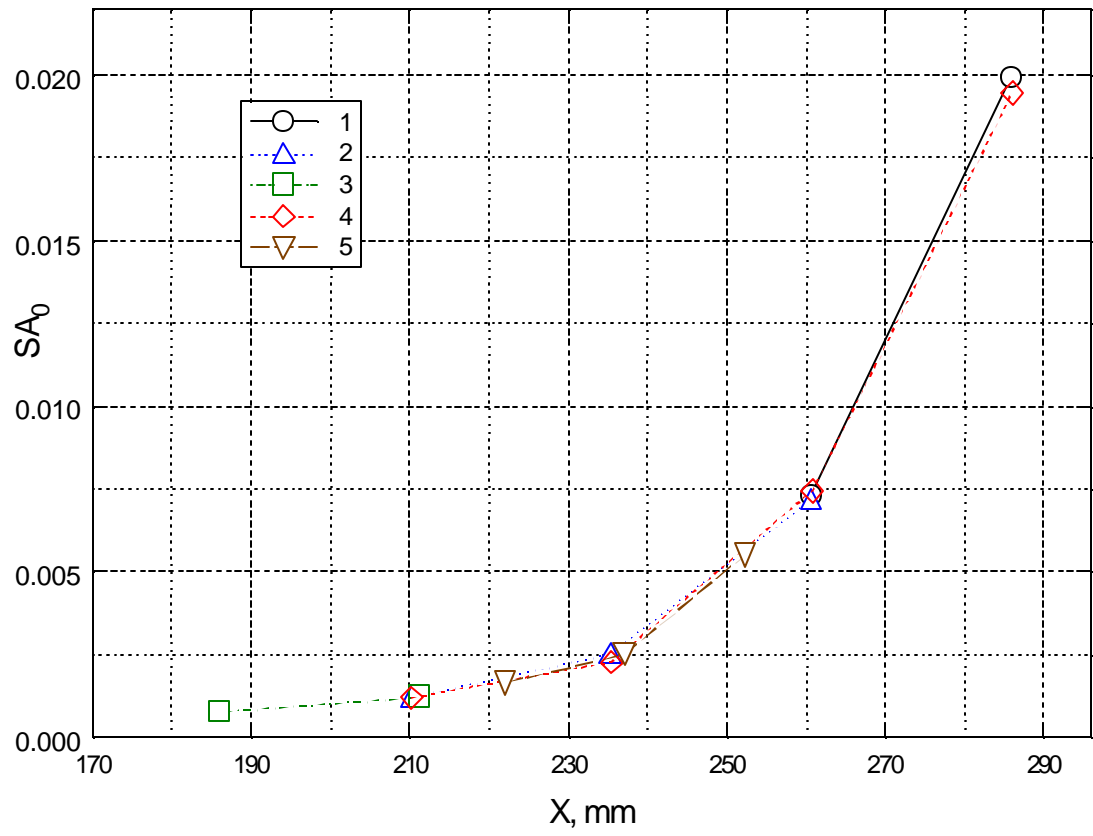
Fig. 46. Normalized longitudinal distributions of wave amplitude for *b*=0 for 5 runs in linear scale.
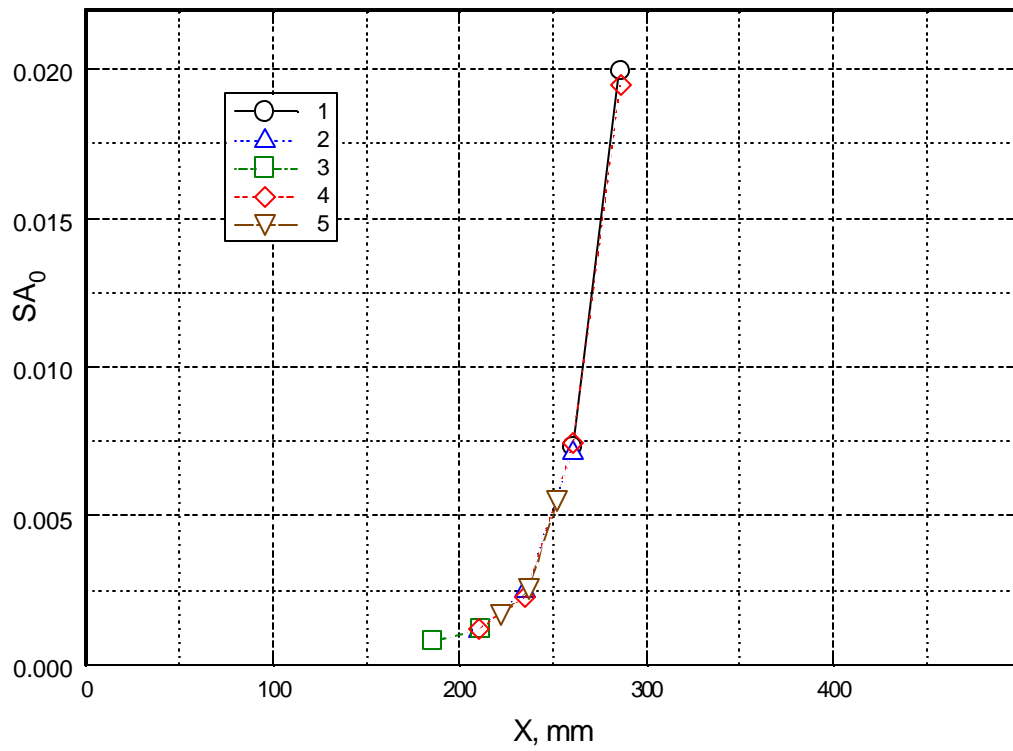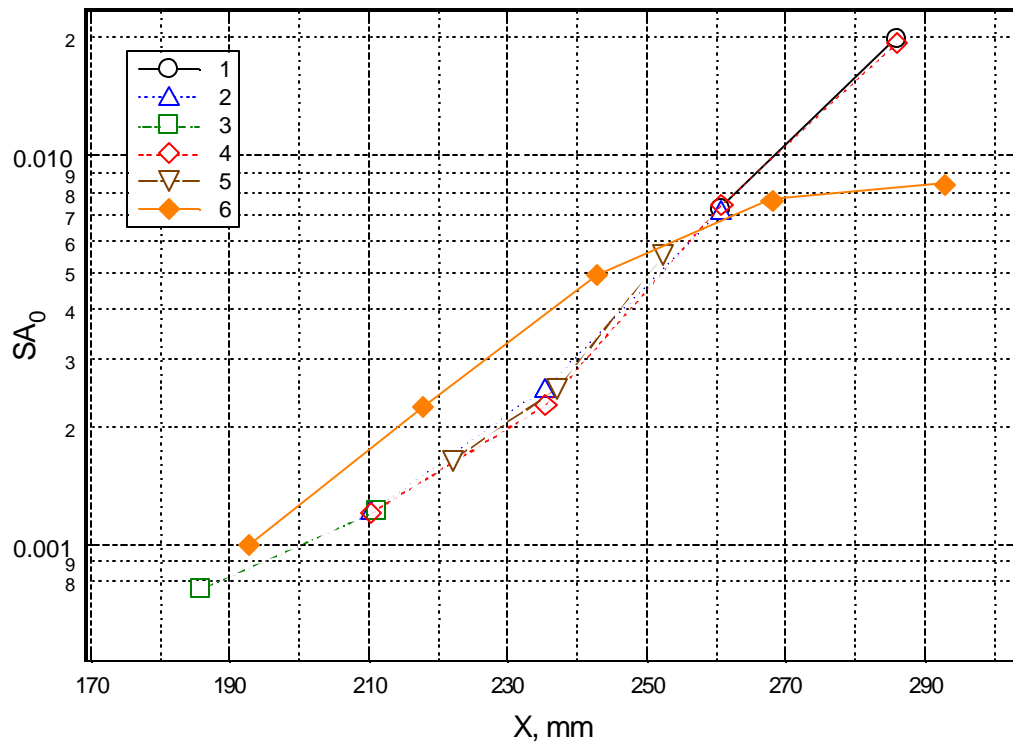
Fig. 48. Comparison of wave amplitude for **b**=0 for sharp (symbols 6) and
blunt (symbols 1-5) cones.

References

1 Mack L.M. 1969. Boundary layer stability theory. Pasadena: Document. JPL No.900-277, Rev. A.

2 Kendall J.M. 1975. Wind tunnel experiments relating to supersonic and hypersonic boundary-layer transition. AIAA J. 13, No.3, 290-299.

3 Demetriades A. 1977. Laminar boundary layer stability measurements at Mach 7 including wall temperature effects. Tech. Report AFOSR-TR-77-1311.

4 Stetson K.F., Thompson E.R., Donaldson J.C. and Siler L.G. 1983. Laminar boundary layer stability experiments on a cone at Mach 8, part 1: sharp cone. AIAA P. 83-1761.

5 Stetson K.F., Thompson E.R., Donaldson J.C. and Siler L.G. 1991. A comparison of planar and conical boundary layer stability and transition at a Mach number of 8. AIAA P. 91-1639.

6 Wendt V., Simen M. 1995. An experimental and theoretical investigation of instabilities in hypersonic flat plate boundary layer flow. Physics of Fluids A, 7 (4): 877-887.

7 Softly E.J. 1969. Boundary layer transition on hypersonic blunt, slender cones. AIAA P. 69-705.

8 Muir J.F., Trujillo A.A. 1972. Experimental investigation of the effects of nose bluntness, free-stream unit Reynolds number, and angle of attack on cone boundary layer transition at a Mach number of 6. AIAA P. 72-216.

9 Stetson K.F. 1979. Effect of bluntness and angle of attack on boundary layer transition on cones and biconic configurations. AIAA P. 79-0269.

10 Stetson K.F., Thompson E.R., Donaldson J.C. and Siler L.G. 1984. Laminar boundary layer stability experiments on a cone at Mach 8, part 2: blunt cone. AIAA P. 84-006.

11 Wilkinson S.P. 1997. A review of hypersonic boundary layer stability experiments in a Quiet Mach 6 Wind Tunnel. AIAA P. 97-1819.

12 Schneider S.P. 2001. Hypersonic laminar instability on round cones near zero angle of attack. AIAA P. 2001-0206.

13 Lachowicz J.T., Chokani N. and Wilkinson S.P. 1996. Hypersonic boundary layer stability over a flared cone in a quiet wind tunnel. AIAA P. 96-0782.

14 Lachowicz J.T., Chokani N. and Wilkinson S.P. 1996. Boundary-layer stability measurements in a hypersonic quiet wind tunnel. AIAA J., v.34, No.12, p.2496-2500.

15 Rotta N.R. 1966. Effects of Nose Bluntness on the Boundary Layer Characteristics of Conical Bodies at Hypersonic Speeds, NYU-AA-66-66.

16 Fingerson L.W., Freymuth P. 1983. Thermal Anemometers. Fluid Mechanics Measurements ed R.J.Goldstein, London: Hemisphere.

17 Chen F.-J., Beckwith I.E. 1985. Comparison of hot-wire measurement techniques in a Mach 3 pilot quiet tunnel. ICIASF'85 record. p.79-85.

18 Comte-Bellot G., Sarma G.R. 2001. Constant voltage anemometer practice in supersonic flows. AIAA J., v.39, No.2, p.261-270.

19 Steson K.F., Kimmel R.L 1992. Example of second-mode instability dominance at a Mach number of 5.2. AIAA J., v.30, No.12, p.2974-2976.